

Reconstruction of Cooperite (PtS) Surfaces: A DFT-D+U Study

Peace P. Mkhonto* and Phuti E. Ngoepe

Cite This: *ACS Omega* 2022, 7, 43390–43410

Read Online

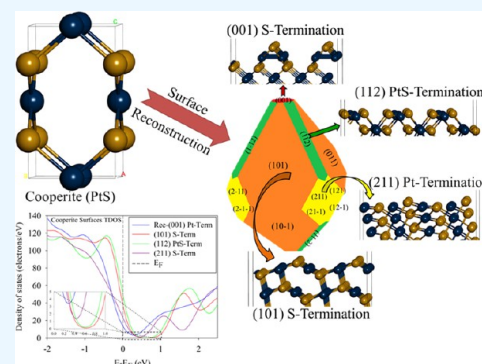
ACCESS |

Metrics & More

Article Recommendations

Supporting Information

ABSTRACT: Cooperite (PtS) is one of the main sources of platinum in the world and has not been given much attention, in particular from the computational aspect. Besides, the surface stability of cooperite is not fully understood, in particular the preferred surface cleavage. In the current study, we employed computer modeling methods within the plane-wave framework of density functional theory with dispersion correction and the U parameter to correctly predict the bulk and surface properties. We reconstructed and calculated the geometries and surface energies of (001), (100), (101), (112), (110), (111), and (211) cooperite surfaces of stoichiometric planes. The Pt d -orbitals with $U = 4.5$ eV and S p -orbitals with $U = 5.5$ eV were found optimum to correctly predict a band gap of 1.408 eV for the bulk cooperite model, which agreed with an experimental value of 1.41 eV. The PtS-, Pt-, and S-terminated surfaces were investigated. The structural and electronic properties of the reconstructed surfaces were discussed in detail. We observed one major mechanism of relaxation of cooperite surface reconstructions that emerged from this study, which was the formation of Pt–Pt bonds. It emanated that the (110) and (111) cooperite surfaces underwent significant reconstruction in which the Pt^{2+} cation relaxed into the surface, forming new Pt–Pt (Pt_2^{2+}) bonds. Similar behavior was perceived for (101) and (211) surfaces, where the Pt^{2+} cation relaxed inward and sideways on the surface, forming new Pt–Pt (Pt_2^{2+}) bonds. The surface stability decreased in the order (101) > (100) \approx (112) > (211) > (111) > (110) > (001), indicating that the (101) surface was the most stable, leading to an octahedron cooperite crystal morphology with truncated corners under equilibrium conditions. However, the electronic structures indicated that the chemical reactivity stability of the surfaces would be determined by band gaps. It was found that the (112) surface had a larger band gap than the other surfaces and thus was a chemical stability competitor to the (101) surface. In addition, it was established that the surfaces had different reactivities, which largely depended on the atomic coordination and charge state based on population atomic charges. This study has shown that cooperite has many planes/surface cleavages as determined by the computed crystal morphology, which is in agreement with experimental X-ray diffraction (XRD) pattern findings and the formation of irregular morphology shapes.



1. INTRODUCTION

Cooperite has been understudied from both computational and experimental aspects, which is ascribed to its high natural floatability (easy to float) compared to sperrylite, which is not amiable to floatation and is by far the largest source of platinum. It has been reported that platinum (Pt) and palladium (Pd) are the most prevalent platinum group elements (PGEs) and constitute about 21% arsenide and 19% sulfides.¹ The common arsenide and sulfide minerals are sperrylite (PtAs_2) and cooperite (PtS), respectively. Although cooperite has high natural floatability, understanding its surface character would be beneficial in unraveling its recovery and predicting its surface morphologies. The cooperite mineral is the most Pt-rich with an ideal composition of PtS and usually contains substantial amounts of Pd and Ni.² The mineral was named after Richard A. Cooper, who first characterized this mineral in 1928.³ Later in 1932, Bannister and Hey further solved the structure of cooperite and corrected its formula based on Debye powder patterns obtained by the rotating specimen method.⁴ Cooperite usually occurs in the form of

irregular grains or, more rarely, crystals of the prismatic pattern.

Currently, the largest worldwide suppliers of platinum and palladium are four major layered igneous intrusions, which are the Bushveld Complex in South Africa, the Stillwater Complex in the U.S.A., the Great Dyke in Zimbabwe, and the Noril'sk/Talnakh Complexes in Russia. The Bushveld Complex is the world's largest layered intrusion, and it has a unique character that makes it the most important layered intrusion of all. The upper critical zone of the Bushveld Complex hosts the largest concentration of PGEs in the world.^{5,6} The upper zone within the northern limb of the Bushveld Complex is composed of Upper Group Chromitite No. 2 (UG-2) and Merensky Reef

Received: May 9, 2022

Accepted: September 8, 2022

Published: November 24, 2022



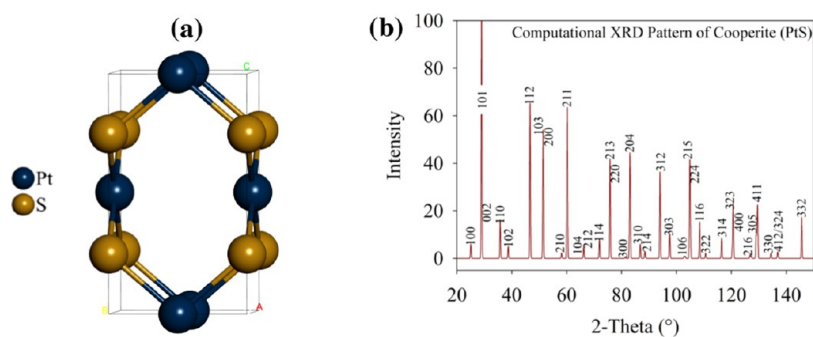


Figure 1. (a) Bulk cooperite crystal model and (b) computational predicted X-ray diffraction pattern of cooperite.

and Platreef mineralization. The major platinum group minerals are cooperite (PtS), braggite ((Pt, Pd)NiS), sperrylite (PtAs₂), and PGE alloys. The platinum group minerals present in the UG-2 Reef are highly variable, but generally, UG-2 is characterized by the presence of abundant PGE sulfides, comprising predominantly laurite (RuOsIr sulfide), cooperite (PtS), and braggite (Pt,Pd)NiS.⁶ It has been reported that the reflectance spectra for cooperite and braggite (Pt,Pd)S from Potgietersrus, South Africa, were measured between 400 and 700 nm.⁷

There is very little information available in terms of cooperite surface studies from the experimental aspect. The experimental study on cooperite morphologies was investigated using a high-resolution electron microscope and Fourier transformation.⁸ The morphology of cooperite was reported as irregular grains with crystal faces or prismatic crystals. The irregular microcrystalline aggregates of cooperite are found in the form of individual grains or sulfide shells surrounding the grains of native platinum. Moreover, the surface study of the crystal faces indicated even perfect surfaces of specimens, surfaces with platinum-enriched microzones, and ultrathin porosity. It has been reported that some crystal zones have a pronounced microblock structure.⁸ Furthermore, high-resolution transmission electron microscopy indicated that the crystal structure of cooperite is characterized by a high degree of order and there were no structural defects in the packing of Pt atoms. In addition, the electron diffraction pattern revealed no superstructure reflections, and the interplanar distances $d_{101} = 0.304$ nm, $d_{011} = 0.308$ nm, $d_{110} = 0.248$ nm, and $d_{112} = 0.196$ nm were determined, where they reported an insignificant deformation of $d_{101} \neq d_{011}$.⁸ Previous studies showed that cooperite displayed many X-ray diffraction (XRD) patterns, which suggested that cooperite has many plane cleavages and therefore forms irregular morphology shapes.^{8–11} It has been reported that during the first stages of the flotation process where mineral particles are crushed, the minerals mainly cleave along surfaces that have large interplanar spacings and few interplanar bonds.¹² These are usually low-index surfaces with low surface energies under dry conditions, and therefore, the large interplanar distance of (101) and (011) may imply dominant planes for cooperite.

Computational methods based on density functional theory have proved to be effective tools to investigate the surface stability and surface reactivity of minerals. The computational available studies have investigated the electronic, structural, and optical properties of cooperite and predicted a nonmetallic semiconducting behavior. Besides, a new set of potential models for the cooperite structure were derived and used to study the pressure dependence of the lattice constant. The

models revealed that cooperite display abnormality under hydrostatic pressure, by expanding along the *c*-lattice constant with increased pressure, although there was no experimental evidence.¹³ Another study investigated the stability of cooperite and its mixture with Pd atoms, where the Pt_{37.5}Pd_{12.5}S₅₀ mixture system was the most stable.¹⁴ Computational methods have been widely used to investigate a wide range of minerals, including pyrite;^{15,16} chalcopyrite;^{17,18} pentlandite;^{19–21} sperrylite, pentlandite, and platinum;²² and sperrylite and platarsite.²³ These also include the reconstruction of different surfaces,^{24,25} oxidation mechanism,^{26–29} and separation of minerals.^{30,31} Nevertheless, there is no computational study that investigated the cooperite surfaces. Surface studies are one of the most important methods to understand the chemical behavior and reactivity of minerals that can be applicable to their recovery. In particular, the prediction and investigation of the interaction of various ligands on the surfaces are well archived through surface studies. However, this may be challenging when a mineral structure that possesses asymmetric dipole surfaces. These types of surfaces require reconstruction as defined by Tasker.³² The reconstructions of surfaces have been previously performed such as on chalcopyrite²⁵ and InAs(001).³³

In this paper, we investigate the surfaces of cooperite and their reconstruction to establish the most preferred cleavage plane, leading to equilibrium crystal morphology prediction from surface energies using density functional theory with dispersion correction and the *U* parameter (DFT-D+*U*). The surfaces considered are (001), (100), (101), (112), (110), (111), and (211) surfaces. The structural and electronic properties and the stability of cooperite surfaces are explored and discussed in detail.

2. COMPUTATIONAL METHODS

In this study, we investigated the bulk, surfaces, and surface reconstructions using density functional theory,^{34,35} with the dispersion correction (DFT-D) method by Tkatchenko and Scheffler (TS).³⁶ The generalized gradient approximation with the Perdew–Burke–Ernzerhof functional (GGA-PBE)³⁷ was employed as implemented within the Cambridge Serial Total Energy Package (CASTEP) code³⁸ of Materials Studio software. The interactions between valence electrons and the ionic core were represented by ultrasoft pseudopotentials, and the valence electron configurations considered for the bulk and surfaces were Pt: [Xe]5d⁹6s¹ and S: [Ne]3s²3p⁴. The plane-wave cutoff energy of 500 eV was found sufficient to converge the total energy of the systems (bulk and surfaces). The *k*-points employed for the bulk and surface were 8 × 8 × 5 and 4 × 4 × 1, respectively, as proposed by Monkhorst–Pack.³⁹ The

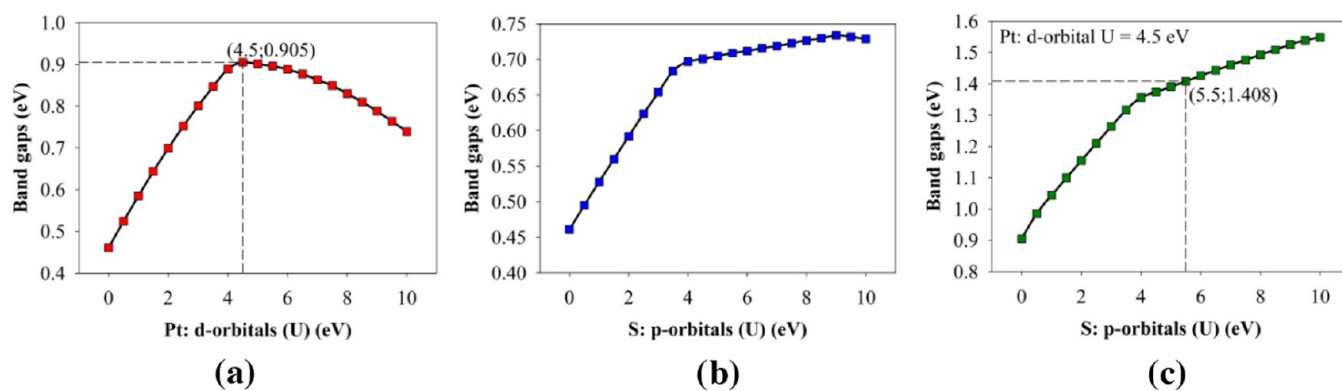


Figure 2. Bulk PtS calculated band gaps as a function of the U parameter: (a) Pt d-orbital U variations, (b) S p-orbital U variations, and (c) Pt d-orbitals = 4.5 eV with S p-orbital U variations.

convergence tolerances for force, ionic displacement, and energy were 0.05 eV/Å, 0.002 Å, and 2.0×10^{-5} eV/atom, respectively.

The bulk model of cooperite is defined by the space group symmetry of $P42/mmc$ (No. 131). The cooperite model belongs to degenerate structures of the CsCl type, each Pt^{2+} atom forms four coplanar bonds, and each sulfur atom forms four tetrahedral bonds. S ions form a tetragonally distorted ($c/2a = 0.88$) simple cubic packing.^{8,40} Due to this geometry of the atomic packing, the model contains large open channels, as shown in Figure 1a. The computational X-ray diffraction (XRD) of cooperite was determined by Reflex module⁴¹ software, as shown in Figure 1b. The computational XRD clearly shows that the highest intensities above 60 emanate from the (101), (112), and (211) planes, which is in agreement with the reported experimental XRD patterns.^{8–11} Interestingly, both (002) and (101) peak intensities are at around $2\theta = 29^\circ$, which has been found experimentally,¹¹ which makes them not easily distinguishable. However, the (002) peak has low intensity compared to the (101) peak, which reached 100 intensity, as shown in Table S1, demonstrating that the (101) plane is the most dominant for cooperite.

A computational study using zero pressure on the cooperite structure previously reported a semiconductor with a direct band gap of 0.4 eV with both the valence maximum and the conduction minimum being located at the M-point.¹³ Another study reported a band gap of ~ 0.32 eV for cooperite.⁴² Nguyen et al. used the tight-binding linear muffin-tin orbital (TB-LMTO) technique and predicted a nonmetallic with a semiconductor band gap of 1.31 eV for cooperite.⁴³ Furthermore, the experimental studies reported a band gap of ~ 1.41 eV using X-ray diffraction,⁴⁴ and band gaps of 0.8 and 1.40 eV were reported using the absorption curve from X-ray diffraction and diffuse reflectance measurement for cooperite.⁴⁵ Recently, a DFT study was conducted to calculate cooperite band gaps using GGA and the Heyd–Scuseria–Ernzerhof hybrid functional (HSE06), where band gaps of 0.43 and 1.58 eV were found, respectively.⁴⁶ As expected, a larger band gap was obtained with the HSE06 approach. It is clear that experiments, TB-LMTO, and DFT using HSE06 established that cooperite had a wide band gap and was a semiconductor. However, standard DFT underestimated the band gap of the cooperite material.

In this study, at 0 K, we used DFT-D with the U parameter to account for the underestimation of band gaps by standard

DFT. We corrected the Pt d-orbital occupancy and delocalization of electrons occurring in the condensed matter transition metal system by the pure DFT functional.^{47–50} This method attempted to correctly predict the band gap of cooperite. Figure 2 shows the calculated band gaps as a function of the U parameter. We observed that as we increase the U values for the Pt d-orbital, the band gap also increases up to 0.905 eV and thereafter begins to decrease. This showed that we could only obtain the highest band gap of 0.905 eV at a U parameter of 4.5 eV, which is lower than the reported experimental band gap (Figure 2a). We therefore varied and examined the effect of U parameters on S p-orbitals and found that as we increased the U parameters, the band gap also increased sharply up to $U = 4.0$ eV and thereafter increased gradually, where the band gap dropped for $U = 9.5$ and 10.0 eV (Figure 2b). In Figure 2c, we used the Pt d-orbital $U = 4.5$ eV parameter, which gave the highest band gap, and varied the S p-orbital U parameter on cooperite and found that the band gap increased and could reach up to 1.549 eV at $U = 10$ eV. Based on experimentally reported band gaps of 1.41 and 1.40 eV for cooperite,^{44,45} we chose $U = 4.5$ eV for Pt d-orbitals and $U = 5.5$ eV for S p-orbitals as working U parameters, which gave a band gap of 1.408 eV for cooperite (Figure 2c), and the computed band structure is shown in Figure S1. This method was found to well correlate with reported band gaps from the experiment and demonstrated that cooperite had a semiconductor character, and these working U parameters were used in all surface calculations. This was significant in determining the oxidation states and spin state of the cooperite material. It is clear that there is a strong bonding between the Pt 5d and S 3p orbitals, playing a crucial role in the formation of the semiconductor band gap for cooperite. In addition, the S p-orbital U parameters had a significant effect in widening the band gap of cooperite that matched with the experimental band gap. The DFT-D+ U relaxed unit cell of the cooperite bulk model, as shown in Figure 1a, was found to have lattice vectors of $a = b = 3.498$ Å and $c = 6.095$ Å, which were in good agreement with experimental cell parameters of $a = 3.47$ and $c = 6.10$ Å determined using X-ray powder diffraction.^{9–11,51}

The surfaces were obtained from a relaxed bulk model of cooperite and modeled using periodic supercells, consisting of eight layers for (001), (100), and (110) surface slabs. For (101), (111), (112), and (211) surface slabs, 12 layers, 18 layers, 5 layers, and 21 layers were adopted, respectively. These slabs were separated by a vacuum space of 20 Å along the Z -direction to avoid spurious interactions between unit cell

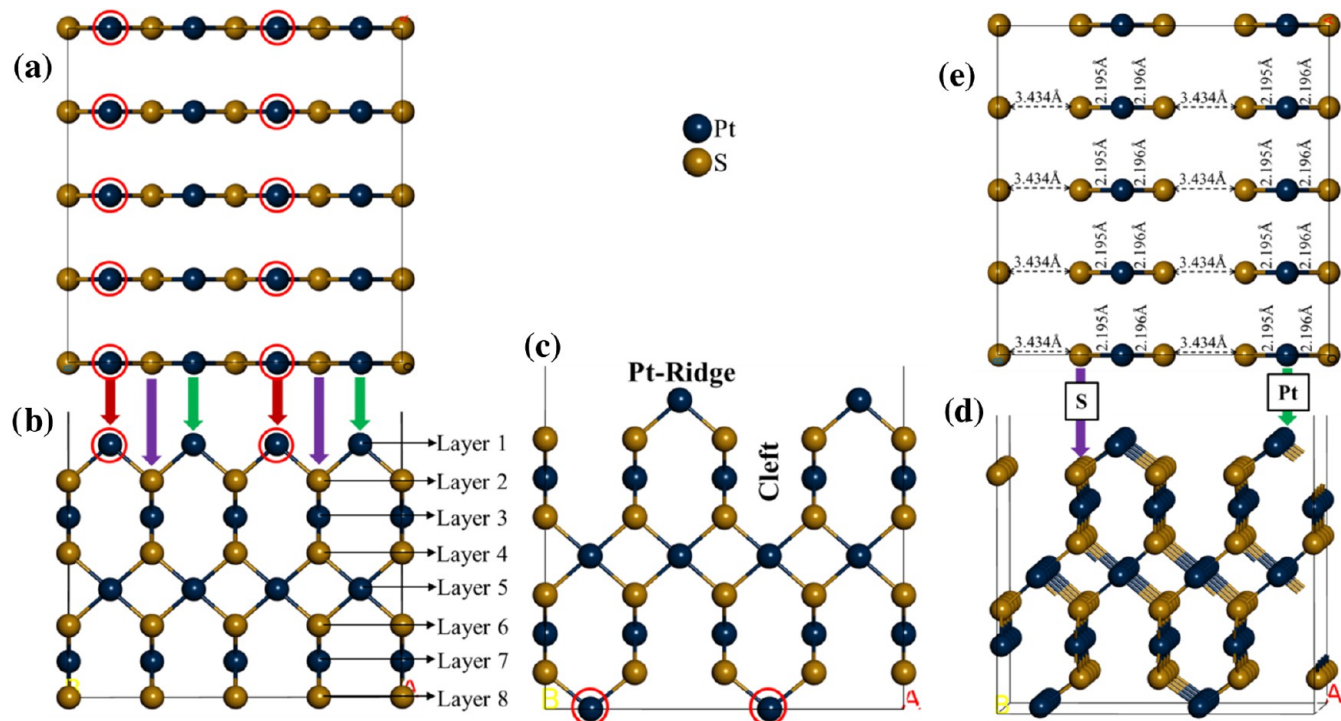


Figure 3. Pt-termination of the (001) surface: (a) view of unreconstructed top two layers, (b) unreconstructed side view, (c) unreconstructed side view, (d) relaxed reconstructed side view, and (e) view of relaxed reconstructed top two layers with bond lengths.

images. The thicknesses of the slab models were determined to give satisfactory convergence and were therefore used in this study. During all geometry optimization calculations, no atoms were kept fixed to bulk coordinates to allow full relaxation of the top and bottom of the surface slabs. We computed structural relaxations on (4×4) , (3×2) , (2×4) , (3×2) , (3×3) , (3×2) , and (2×2) supercells for (001), (100), (101), (112), (110), (111), and (211) surfaces, respectively. We carried out energy minimizations of all surface slabs to obtain their surface energies. We computed the surface energies of the unreconstructed surfaces ($E_{\text{Surf}}^{\text{U}}$) from single point energy calculations of the pristine asymmetric and symmetric and reconstructed symmetric stoichiometric slabs using eq 1^{52–55}

$$E_{\text{Surf}}^{\text{U}} = \frac{E_{\text{Slab}}^{\text{U}} - nE_{\text{Bulk/atom}}}{2A} \quad (1)$$

where ($E_{\text{Slab}}^{\text{U}}$) is the total energy of the unreconstructed slab, $E_{\text{Bulk/atom}}$ is the energy of the bulk per number of atoms, n is the number of atoms in the slab, and A is the surface area multiplied by 2 to account for the top and bottom surface areas. The unreconstructed and reconstructed surface energies of the relaxed slabs ($(E_{\text{Surf}}^{\text{R}})$) were also computed using eq 2,^{30,52,53} similar to eq 1

$$E_{\text{Surf}}^{\text{R}} = \frac{E_{\text{Slab}}^{\text{R}} - nE_{\text{Bulk/atom}}}{2A} \quad (2)$$

where ($E_{\text{Slab}}^{\text{R}}$) is the total energy of the unreconstructed slab, $E_{\text{Bulk/atom}}$ is the energy of the bulk per number of atoms, n is the number of atoms in the slab, and A is the surface area multiplied by 2 to account for the top and bottom surface areas. Note that the lowest positive surface energy depicts the most thermodynamically stable surface. We also calculated the degree of relaxation of each surface as a percentage using eq 3⁵⁵

$$\text{Relaxation} = \frac{E_{\text{Surf}}^{\text{U}} - E_{\text{Surf}}^{\text{R}}}{E_{\text{Surf}}^{\text{U}}} \times 100 \quad (3)$$

The surface energy change between the unreconstructed and reconstructed surface slabs from the surface energies was computed using eq 4

$$\Delta E_{\text{Surf}} = E_{\text{Surf}}^{\text{Rec.}} - E_{\text{Surf}}^{\text{Unrec.}} \quad (4)$$

where a negative value indicates stability exothermic formation of the reconstructed surface, while a positive value denotes the opposite. The vertical displacement of the top layer atoms was computed using eq 5

$$\Delta d_z = d_{z(\text{R})} - d_{z(\text{U})} \quad (5)$$

where $d_{z(\text{U})}$ and $d_{z(\text{R})}$ are the Z-atomic positions for the unreconstructed and relaxed surfaces, respectively. Negative and positive values show inward and outward displacements, respectively.

Previous studies have shown that using surface energies to calculate crystal morphologies provides good agreement with the experiment, as the difference in entropy between the bulk and the surface is small.^{56,57} As such the equilibrium morphology of the cooperite crystal is constructed according to Wulff's theorem,⁵⁸ where the distance from the center of the particle to the surface is proportional to the surface energy. The morphology is determined by the surface energies and the related growth rates of the various surfaces, which provides a measure of the relative stabilities of the surfaces.⁵⁵ This method is based on the Gibbs approach,⁵⁹ who proposed that under thermodynamic control, the equilibrium form of a crystal should possess minimal total surface free energy for a given volume.

3. RESULTS

There are three types of surfaces that were described by Tasker,³² as shown in Figure S4, for the surface stability of an ionic covalent compound such as cooperite. In Type I, each layer is neutral with a relative number of cations and anions, making the overall charge equal to zero. Type II presents charged layers without perpendicular charge due to the stacking sequence, and Type III is charged with an electrostatic dipole perpendicular to the surface plane (see Figure S4). Tasker³² also reported that Type I and II surfaces can exist in nature with only small relaxation and reconstruction, while Type III requires considerable reconstruction to disperse the net charge.

In the next sections, we discuss the reconstructions of (001), (100), (110), and (111) surfaces. It is important to emphasize that cooperite has an important covalent character with large Type III surfaces and requires reconstruction. Different terminations of the lower-Miller-index surfaces (001), (100), (101), (112), (110), (111), and (211) of cooperite were modeled, and we found that the (001), (100), (111), and (110) surfaces had two terminations that were of Type III and required reconstruction. The (101) and (211) surfaces had three terminations that were of Type II, while the (112) surface had only one termination that was of Type I. The unstable cleavage planes in cooperite are shown in the Supporting Information (Section SI 3), while the reconstructed and nondipole stable surfaces are discussed in detail in the following sections. Note that on the relaxed surfaces, the Pt-S and Pt-Pt bond lengths were compared with the Pt-S = 2.350 Å and Pt-Pt = 2.700 Å bond lengths, respectively, obtained from the sum of the empirically measured covalent radii of Pt (1.350 Å) and S (1.00 Å) atoms determined by Slater.⁶⁰

3.1. (001) Surface (4 × 4) Supercell. The cooperite (001) surface is composed of Pt-terminated and S-terminated surfaces, which were modeled and reconstructed using a 4 × 4 supercell. The unreconstructed (001)-Pt-Term surface has, in its first atomic layer (layer 1), 16 Pt atoms and 16 S atoms in the second atomic layer (Layer 2), as shown in Figure 3a,b. The unreconstructed and relaxed structures of the unreconstructed surface are shown in Figure S5. We observed that the unreconstructed surfaces do not show any obvious change in structural relaxation, and we found that all Pt-S bonds are 2.203 and 2.204 Å (Figure S5c), a decrease from 2.320 Å. We reconstructed the Pt-Term surface by moving eight Pt atoms circled in red (see Figure 3b) to the bottom of the slab, to create a stoichiometric and symmetric surface slab, as shown in Figure 3c. The reconstruction created a deep cleft that exposes the Pt atoms in layer 5, with the top layer Pt atoms forming a Pt-Ridge.

The relaxed reconstructed Pt-Term surface, as shown in Figure 3d, relaxes the Pt atoms in layer 1 inward, while the S atoms in layer 2 are slightly relaxed outward, as displayed in Table 1. The relaxed bond lengths of the top two exposed atomic layers are shown in Figure 3e. We noted that on the unreconstructed reconstructed Pt-Term surface, the Pt-S bonds are 2.320 Å on the Pt-Ridge, while on the relaxed surface, the bond lengths decreased to 2.195 and 2.196 Å, as indicated in Figure 3e. These were slightly shorter than the Pt-S bonds of 2.203 and 2.204 Å found for the relaxed unreconstructed Pt-Term surface, suggesting stability. In addition, these Pt-S bond lengths were shorter than the Pt-S bond length (2.350 Å)

Table 1. Atomic Vertical Displacements (Δd_z , Å) of the Top Layers on Reconstructed (001) and (100) Surface Models, Obtained from the Unrelaxed ($d_{z(U)}$) and Relaxed ($d_{z(R)}$) Z-Atomic Positions^a

Reconstructed (001) surface					
Rec-Pt-Term			Rec-S-Term		
layer	species	Δd_z	layer	species	Δd_z
layer 1	Pt	-0.0074	layer 1	S	-0.0032
layer 2	S	+0.0001	layer 2	Pt	-0.0020
Reconstructed (100) surface					
layer 1	Pt1	-0.0045	layer 1	Pt1	-0.0083
	S1	-0.0022	layer 2	Pt2	-0.0004
layer 2	Pt2	-0.0008		S1	-0.0048
layer 3	Pt3	-0.0012		S2	+0.0039
	S2	+0.0003	layer 3	Pt3	+0.0050
				Pt4	-0.0043

^aNegative and positive values show inward and outward displacements, respectively.

determined from the sum of the atomic radii, which suggested Pt-S stable bonds.

The unreconstructed S-Term of (001) surface has 16 Pt atoms in layer 1 and 16 S atoms in layer 2, as shown in Figure 4a,b. As shown in Figure S5e, the relaxed unreconstructed S-Term surface clearly showed no obvious change in structural relaxation. In this relaxation, Pt-S bonds of 2.334–2.347 Å were found, which decreased from 2.320 Å. The reconstruction of the S-Term surface required orientation of the cell to view along the O-point such that the OA and OB vector sides are accessible (see Figure 4b). The reconstruction of the S-Term surface was performed by moving eight S atoms circled in red (see Figure 4a,b) to the bottom of the slab to create a stoichiometric and symmetric surface slab, as shown in Figure 4c. The reconstruction creates clefts that exposes the S atoms in layer 3, with the top layer 1 S atoms forming a S-Ridge. The relaxed reconstructed S-Term surface, as shown in Figure 4d, was noted to relax the S atoms in layer 1 inward by -0.0032 Å and the Pt atoms in layer 2 inward by -0.0020 Å, as displayed in Table 1. The relaxed bond lengths of the top two exposed atomic layers are shown in Figure 4e. It is clear from Figure 4d that after relaxation, there is no obvious change in the relaxation of the atoms. We found that the unreconstructed reconstructed S-Term surface had Pt-S bonds with a length of 2.320 Å on the S-Ridge, while the relaxed surface resulted in an increased bond length of 2.277 Å, as indicated in Figure 4e. These Pt-S bonds are shorter than the unreconstructed surface Pt-S bonds of 2.334–2.347 Å, suggesting stability. By comparing the Pt-S bond lengths with the Pt-S bond length (2.350 Å) determined from the sum of the atomic radii, we found that they were shorter, which suggested Pt-S stable bonds.

3.2. (100) Surface (3 × 2) Supercell. Unlike the (001) surface, the (100) surface possesses PtS-terminated and Pt-terminated surfaces, which were reconstructed using a 3 × 2 supercell. The unreconstructed PtS-Term of the (100) surface has, in its first atomic layer, 12 S atoms and 6 Pt atoms, while the second atomic layer is composed of 6 Pt atoms, as shown in Figure 5a,b.

The relaxed surface models of the unreconstructed are shown in Figure S6, and we observed that the surfaces do not show any obvious structural change after relaxation. We noted that the Pt-S bonds on the unreconstructed PtS-termination

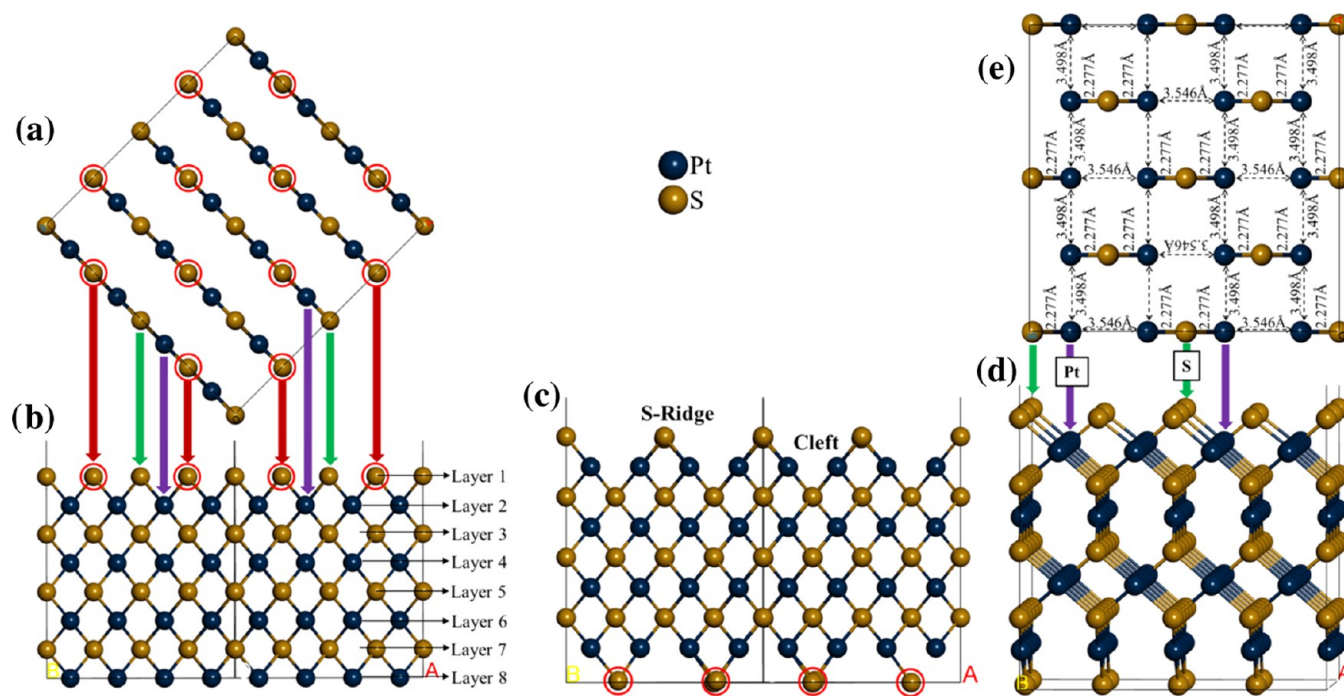


Figure 4. S-termination of the (001) surface: (a) view of unrelaxed unreconstructed top two layers, (b) unrelaxed unreconstructed side view, (c) unrelaxed reconstructed side view, (d) relaxed reconstructed side view, and (e) relaxed reconstructed top two layers view with bond lengths.

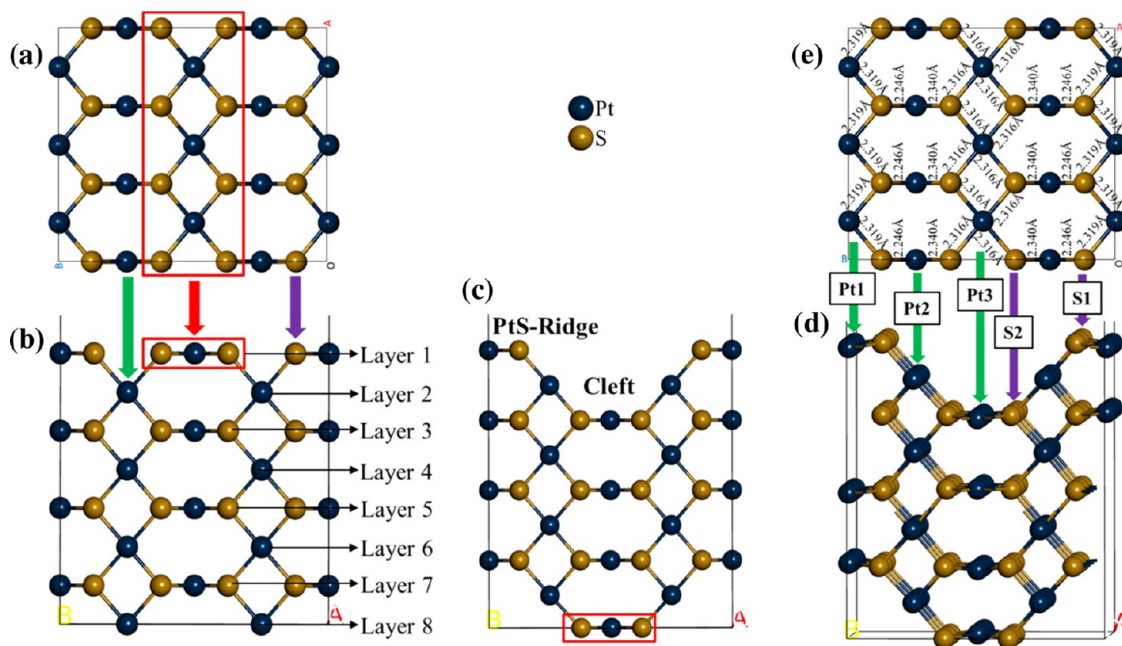


Figure 5. PtS-termination of the (100) surface: (a) view of unrelaxed unreconstructed top two layers, (b) unrelaxed unreconstructed side view, (c) unrelaxed reconstructed side view, (d) relaxed reconstructed side view, and (e) view of relaxed reconstructed top three layers with bond lengths.

surface decreased from 2.320 Å to between 2.258 and 2.316 Å for the top first layers (Figure S6c). We reconstructed the PtS-Term surface by moving the S and Pt atoms in the red rectangle (see Figure 5a,b) to the bottom of the slab to create a stoichiometric and symmetric surface slab, as shown in Figure 5c. The reconstruction created a cleft that exposes S and Pt atoms in layer 3, which is the same as the PtS-Ridge of the slab. The relaxed reconstructed PtS-Term surface, as shown in Figure 5d, was noted to relax the Pt and S atoms inward, except for S2 atoms, which slightly relaxed outward, as

displayed in Table 1. The relaxed bond lengths of the top three exposed atomic layers are shown in Figure 5e. We noted that the unrelaxed reconstructed PtS-Term surface is composed of Pt-S bonds of 2.320 Å on the PtS-Ridge, Cleft floor, and Cleft sides. We found that the relaxed surface resulted in a slight decrease in bond lengths to 2.319 Å on the PtS-Ridge and 2.316 Å on the Cleft floor and an increase to 2.340 and 2.346 Å on the Cleft sides, as indicated in Figure 5e. It is clear that the Pt-S bonds on the Cleft sides increased largely. It was found that the Pt-S bond lengths on the reconstructed surface

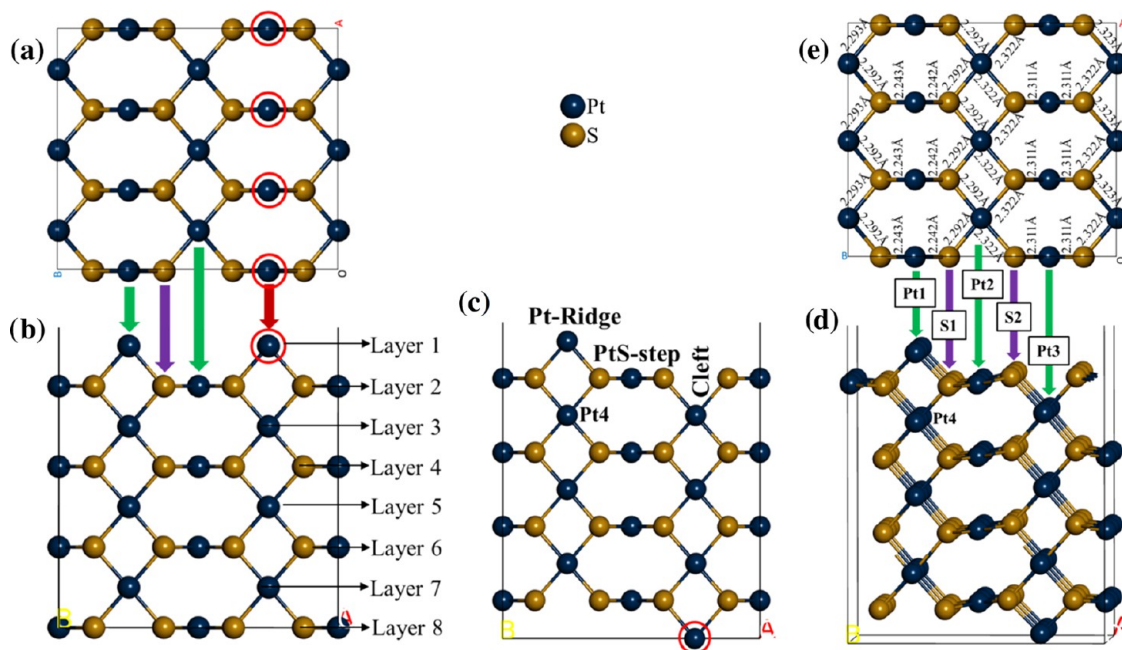


Figure 6. Pt-termination of the (100) surface: (a) view of unreconstructed top two layers, (b) unreconstructed side view, (c) unreconstructed side view, (d) relaxed reconstructed side view, and (e) view of relaxed reconstructed top three layers with bond lengths.

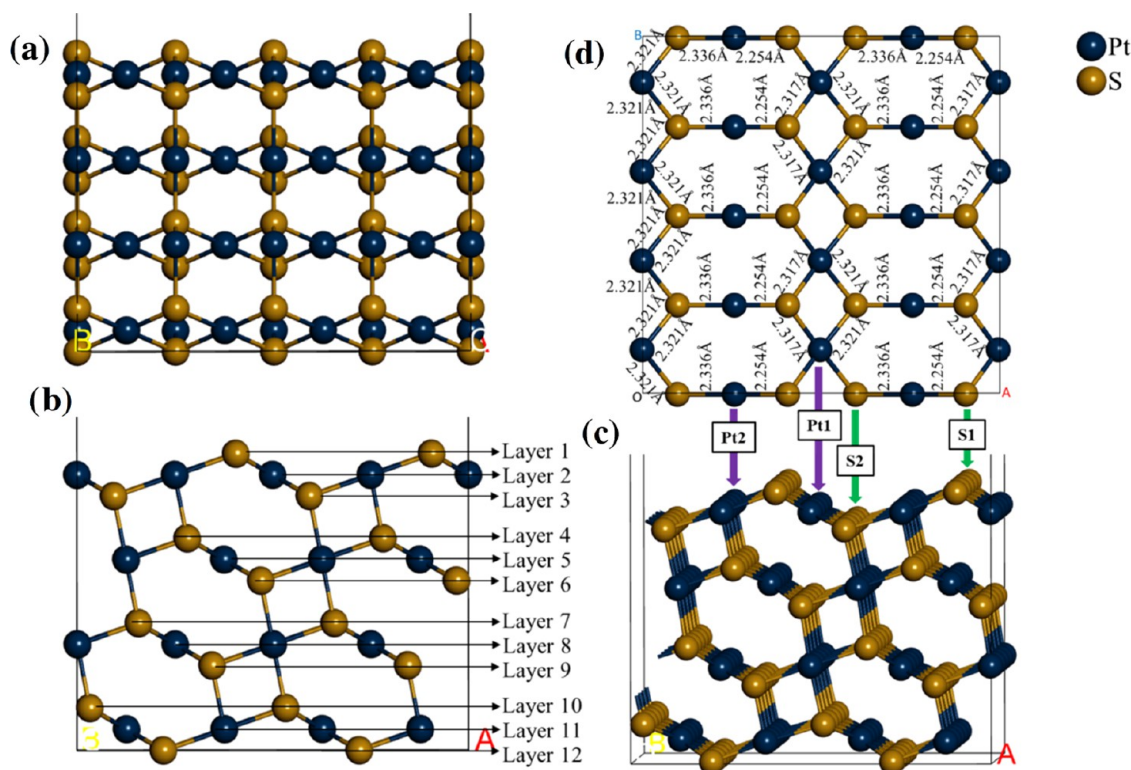


Figure 7. S-termination of the (101) surface: (a) unreconstructed side view, (b) unreconstructed side view, (c) relaxed side view, and (d) view of relaxed top three layers with bond lengths.

were similar to those on the unreconstructed surface and all were shorter than the Pt-S bond length of 2.350 Å determined from the sum of the atomic radii, which suggested Pt-S stable bonds.

The unreconstructed Pt-Term of the (100) surface has, in its first atomic layer, 6 Pt atoms, while the second atomic layer is composed of 6 Pt and 12 S atoms, as shown in Figure 6a,b.

The relaxed structure of the unreconstructed surface is shown in Figure S6e, illustrating that there was no significant structural change after relaxation.

We found that the Pt-S bond lengths decreased from 2.320 to 2.297, 2.300, and 2.310 Å and increased to 2.344 Å, as shown in Figure S6f. We reconstructed the Pt-Term surface by moving the three Pt atoms circled in red (see Figure 6b) to the

bottom of the slab, which creates a stoichiometric and symmetric surface slab, as shown in Figure 6d. The reconstruction created a small cleft that exposes the Pt atoms in the third atomic layer as such the surface is fashioned in Pt-Ridge, Cleft, and PtS-step. Now, the relaxed reconstructed Pt-Term surface displayed an inward relaxation of the first layer Pt1 atoms largely by -0.0083 \AA (Table 1). The Pt2 and S1 atoms in layer 2 also relaxed inward, while the S2 atoms relaxed outward. The Pt3 and Pt4 atoms in layer 3 relaxed outward and inward, respectively, as indicated in Table 1. The relaxed bond lengths of the top three exposed atomic layers are shown in Figure 6e. We noted that on the unrelaxed reconstructed Pt-Term surface, the Pt-S bonds are 2.320 \AA on the Pt-Ridge, Cleft, and PtS-step. It was found that on the relaxed surface, the bond lengths decreased to 2.243 and 2.242 \AA on the Pt-Ridge and decreased to 2.311 \AA on the Cleft, while on the PtS-step, the bond length increased to 2.322 \AA and decreased to 2.292 \AA , as indicated in Figure 6e. It is clear that the Pt-S bond lengths on the Pt-Ridge are shorter than the bond lengths on the unreconstructed surface and on the Cleft and Pt-step for the constructed surface, which suggested that the Pt-Ridge is more stable. In addition, we found that all of the bond lengths were shorter than the Pt-S bond length of 2.350 \AA determined from the sum of the atomic radii, which suggested Pt-S stable bonds.

3.3. (101) Surface (2×4) Supercell. The (101) surface has three terminations, two S-termination (S-Term and S-Term-B) and Pt-termination, which were modeled using a 2×4 supercell. We noted that the reconstruction of S-Term-B and Pt-Term would create the S-Term model; thus, no reconstruction was performed. Moreover, we found that S-Term did not require any reconstruction, since it was of Type II, a nondipole surface slab as described by Tasker.³²

The Pt-Term of the (101) surface has 16 Pt atoms in its first atomic layer and 8 S atoms in the second atomic layer, as shown in Figure S7. After surface relaxation, we observed an inward relaxation of the Pt atoms, which resulted in bond breakage between Pt (layer 1) and S atoms (layer 2), leaving distances of 3.421 , 3.677 , 2.753 , 3.644 , 3.591 , and 3.421 \AA . However, three Pt atoms were still bonded to S atoms, giving bond distances of 2.450 , 2.366 , and 2.384 \AA , which were larger than the Pt-S bond length of 2.350 \AA determined from the sum of the atomic radii, which suggested weaker bonds. These relaxations caused the formation of new Pt-Pt (Pt_2^{2+}) bonds of lengths between 2.656 and 2.784 \AA on the top surface, as shown in Figure S7. These Pt-Pt bond lengths were shorter and larger than the Pt-Pt bond length of 2.700 \AA determined from the sum of the atomic radii, suggesting stronger and weaker Pt-Pt bonds, respectively. We noted that the Pt-S bonds on the top layers decreased from 2.320 \AA to bond distances between 2.225 and 2.317 \AA . These Pt-S bond lengths were shorter than the Pt-S bond length of 2.350 \AA determined from the sum of the atomic radii, which suggested stronger bonds. The bottom surface did not show any significant change after relaxation (see Figure S7b).

The nondipole symmetric S-Term of the (101) surface is composed of 8 S atoms in its first and third atomic layers and 16 Pt atoms in the second atomic layer (Figure 7). The relaxation of S-Term displayed an inward relaxation of the Pt1, Pt2, and S1 atoms on the top two layers, while the S2 atoms in layer 3 slightly relaxed outward, as shown in Table 2. We noted that the unrelaxed S-Term surface is composed of Pt-S bonds with a length of 2.320 \AA , while on the relaxed surface, the bond

Table 2. Atomic Vertical Displacements (Δd_z , \AA) of the Top Layers on the (101) and (112) Surface Models, Obtained from the Unrelaxed ($d_{z(U)}$) and Relaxed ($d_{z(R)}$) Z-Atomic Positions^a

(101) surface			(112) surface		
layer	species	Δd_z	layer	species	Δd_z
layer 1	S1	-0.0022	layer 1	Pt	-0.0069
layer 2	Pt1	-0.0027		S	-0.0008
	Pt2	-0.0025			
layer 3	S2	$+0.0001$			

^aNegative and positive values show inward and outward displacements, respectively.

lengths decreased to 2.254 \AA and increased to 2.317 , 2.321 , and 2.336 \AA , as indicated in Figure 7d. S-Term-B, as shown in Figure S8, has 8 S atoms in the first, second, and fourth atomic layers and 16 Pt atoms in the third atomic layer. S-Term-B is the opposite flip top to bottom of Pt-Term, they have similar orientations, and their relaxations are similar. In this case (S-Term-B), the top surface did not show any significant change after relaxation, where the Pt-S bonds between layers 1 and 3 ranged from 2.294 and 2.327 \AA , as shown in Figure S8d. However, the bottom of the S-Term-B slab formed new Pt-Pt bonds (average 2.645 \AA) as a result of Pt and S bond breakage (Figure S8c). This Pt-Pt bond was shorter than the Pt-Pt bond length of 2.700 \AA determined from the sum of the atomic radii, which suggested Pt-Pt stable bonds. As illustrated in Figure S8d, the Pt-S bond lengths changed from 2.320 \AA to various Pt-S bond lengths between 2.321 and 2.350 \AA (see Figure S8d for other bond lengths). The Pt-S bond lengths on S-Term and S-Term-B were similar, with those from S-Term-B slightly larger, suggesting that S-Term was more stable. All these Pt-S bond lengths were shorter than the Pt-S bond length of 2.350 \AA determined from the sum of the atomic radii, which suggested Pt-S stable bonds.

3.4. (112) Surface (3×2) Supercell. The (112) surface has only one termination, that is, PtS-termination, which was modeled using a 3×2 supercell. We found that PtS-Term did not require any reconstruction, since it was of Type I (nondipole surface slab). The first top layer (layer 1) is composed of 12 S and Pt atoms (Figure 8d). The relaxation of PtS-Term displayed an inward relaxation of the Pt and S atoms, as shown in Table 2 (also see Figure 8c), where Pt atoms relaxed inward largely by -0.0069 \AA compared to S atoms (-0.0008 \AA). The bond lengths of the top first layer are shown in Figure 8d. We noted that on the unrelaxed surface, the Pt-S bonds were 2.320 \AA , while on the relaxed surface, the bond lengths decreased to 2.277 \AA and increased to 2.328 \AA , as shown in Figure 8c. These Pt-S bond lengths were shorter than the Pt-S bond length of 2.350 \AA determined from the sum of the atomic radii, which suggested stable Pt-S bonds.

3.5. (110) Surface (3×3) Supercell. Similar to the (001) surface, the (110) surface is also composed of Pt-terminated and S-terminated surfaces, which were modeled and reconstructed using a 3×3 supercell. The unreconstructed S-Term of the (110) surface has 18 Pt atoms in layer 1 and 18 S atoms in layer 2, as shown in Figure 9a,b. The relaxed structure of the unreconstructed S-Term surface is shown in Figure S9c,d. The top of the unreconstructed S-Term surface did not show any obvious relaxation changes and the Pt-S bond lengths changed from 2.320 \AA to between 2.302 and

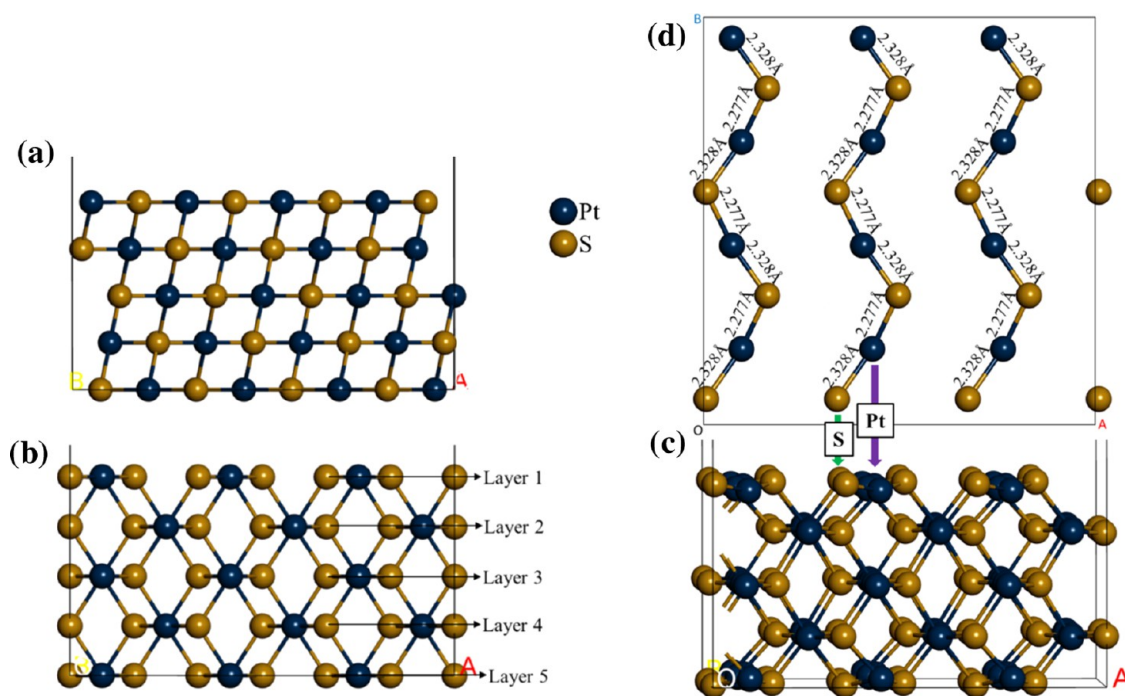


Figure 8. PtS-termination of the (112) surface: (a) unrelaxed OB vector side view, (b) unrelaxed OA vector side view, (c) relaxed OA vector side view, and (d) relaxed top layer view with bond lengths.

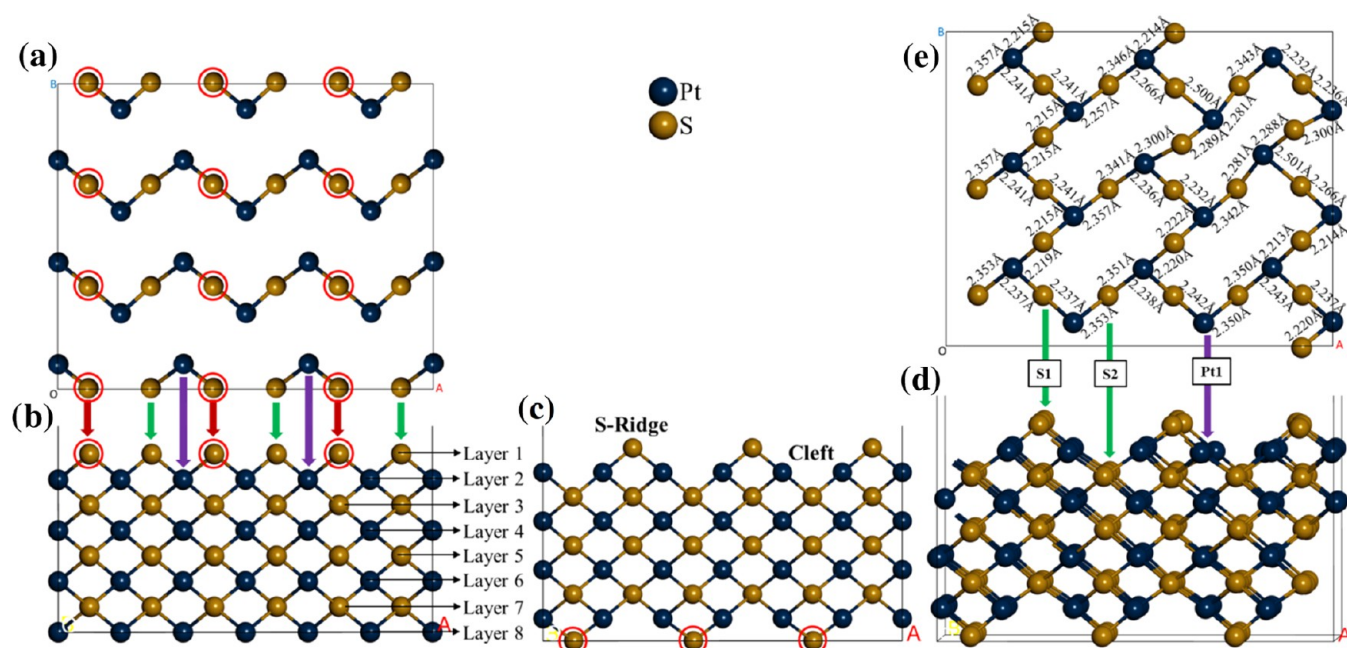


Figure 9. S-termination of the (110) surface: (a) view of unrelaxed unreconstructed top two layers, (b) unrelaxed unreconstructed side view, (c) unrelaxed reconstructed side view, (d) relaxed reconstructed side view, and (e) view of relaxed reconstructed top three layers with bond lengths.

2.311 Å. We observed a drastic relaxation of the bottom side of the slab, whereby layer 8 moved and almost aligned with layer 7 and formed new Pt-Pt bonds (Pt_2^{2+}). We noted four Pt-Pt bonds with an average length of 2.703 Å within layer 8 (see Figure S9f), which is slightly larger than the Pt-Pt bond length of 2.700 Å determined from the sum of the atomic radii. Now, we reconstructed the S-Term surface by moving nine S atoms circled in red (see Figure 9b) to the bottom of the slab, which resulted in a stoichiometric and symmetric surface slab, as shown in Figure 9c. The reconstruction created a cleft that

exposes the S atoms in layer 3, with the S atoms in layer 1 forming a S-Ridge. As shown in Figure 9d, the S1 and Pt atoms in layers 1 and 2 relaxed inward, respectively, while the S2 atoms in layer 3 relaxed outward, as displayed in Table 3. The relaxed bond lengths of the top three exposed atomic layers are shown in Figure 9e. We noted that the unrelaxed reconstructed S-Term surface was composed of Pt-S bonds with a length of 2.320 Å on the S-Ridge and Cleft, which were found to range between 2.215 and 2.500 Å on the S-Ridge and ranged between 2.281 and 2.357 Å on the Cleft for the relaxed surface

Table 3. Atomic Vertical Displacements (Δd_z , Å) of the Top Layers on Reconstructed (110) Surface Models, Obtained from the Unrelaxed ($d_{z(U)}$) and Relaxed ($d_{z(R)}$) Z-Atomic Positions^a

Rec-(110) surface					
Pt-termination			S-termination		
layer	species	Δd_z	layer	species	Δd_z
layer 1	Pt1	-0.0262	layer 1	S1	-0.0037
layer 2	S1	+0.0024	layer 2	Pt1	-0.0032
layer 3	Pt2	+0.0017	layer 3	S2	+0.0020
	Pt3	-0.0014			

^aNegative and positive values show inward and outward displacements, respectively.

(Figure 9e). We observed that the Pt-S bond lengths on the reconstructed surface ranged from shorter bond lengths compared to the unreconstructed surface. However, the reconstructed surface formed some large Pt-S bonds with a length of 2.500 Å, which were larger than the Pt-S bond length of 2.350 Å determined from the sum of the atomic radii, which suggested relaxation instability of the reconstructed surface compared to the unreconstructed surface.

Now, we examine the relaxed structure of the unreconstructed Pt-Term surface, as shown in Figure S10 in the Supporting Information. Note that the unreconstructed Pt-Term of the (110) surface has 18 Pt atoms in its first atomic layer and 18 S atoms in the second atomic layer, as shown in Figure 10a,b. We observed that on the unreconstructed Pt-Term surface, layer 1 relaxed inward drastically and reconstructed, forming new Pt-Pt (Pt_2^{2+}) bonds. This relaxation resulted in layer 1 forming Pt-Pt bond lengths between 2.674 and 2.751 Å, which were shorter and larger than the Pt-Pt bond length of 2.700 Å determined from the sum of the atomic radii, suggesting stronger and weaker Pt-Pt bonds, respectively (see Figure S10e). We found that the Pt-S bond lengths on the relaxed unreconstructed Pt-Term surface changed from 2.320 Å to bond lengths between 2.252 and

2.541 Å. These Pt-S bond lengths were shorter and larger than the Pt-S bond length of 2.350 Å determined from the sum of the atomic radii, which suggested stronger and weaker bonds. This suggested an unstable surface relaxation of the unreconstructed surface. The bottom side did not show any significant relaxation (Figure S10c,d).

In the case of reconstruction of Pt-Term, the nine Pt atoms circled in red (see Figure 10b) were moved to the bottom of the slab, consequently resulting in a stoichiometric and symmetric surface slab, as shown in Figure 10d. The reconstruction created clefts that exposed the Pt atoms in layer 3, while the Pt atoms in layer 1 formed a Pt-Ridge. From the relaxed reconstructed Pt-Term surface, as shown in Figure 10e, we observed that layer 1 relaxed inward largely by -0.0262 Å (Table 3). This resulted in self-reconstruction and created new Pt-Pt bonds of 2.744 Å (Pt1-Pt3) between layers 1 and 3, which aligned with S atoms in layer 2, thus creating a flat PtS-Ridge (see Figure 10e). We found that S1 atoms in layer 2 relaxed outward. The third layer (layer 3) had two Pt atoms that relaxed differently (Pt2 and Pt3), and it was found that Pt2 atoms relaxed outward, while Pt3 atoms relaxed inward, as displayed in Table 3 (also see Figure 10e for atom naming). Similar relaxation was observed at the bottom of the surface (Figure 10e). The relaxed bond lengths of the top three exposed atomic layers are shown in Figure 10f. We noted that on the unrelaxed reconstructed Pt-Term surface, the Pt-S bond lengths were 2.320 Å on the Pt-Ridge and Cleft, while on the relaxed surface, the bond lengths decreased to 2.237 Å and increased to 2.330 Å on the flat PtS-Ridge (Figure 10f). These Pt-S bond lengths were shorter than the Pt-S bond length of 2.350 Å determined from the sum of the atomic radii, which suggested surface relaxation stability.

3.6. (111) Surface (3 × 2) Supercell. The cooperite (111) surface is also Pt-terminated and S-terminated, which were modeled and reconstructed using a 3 × 2 supercell. The reconstruction of Pt-Term was carried out by moving the three Pt atoms circled in red (see Figure 11a,b) to the bottom of the slab, creating a stoichiometric and symmetric surface slab, as

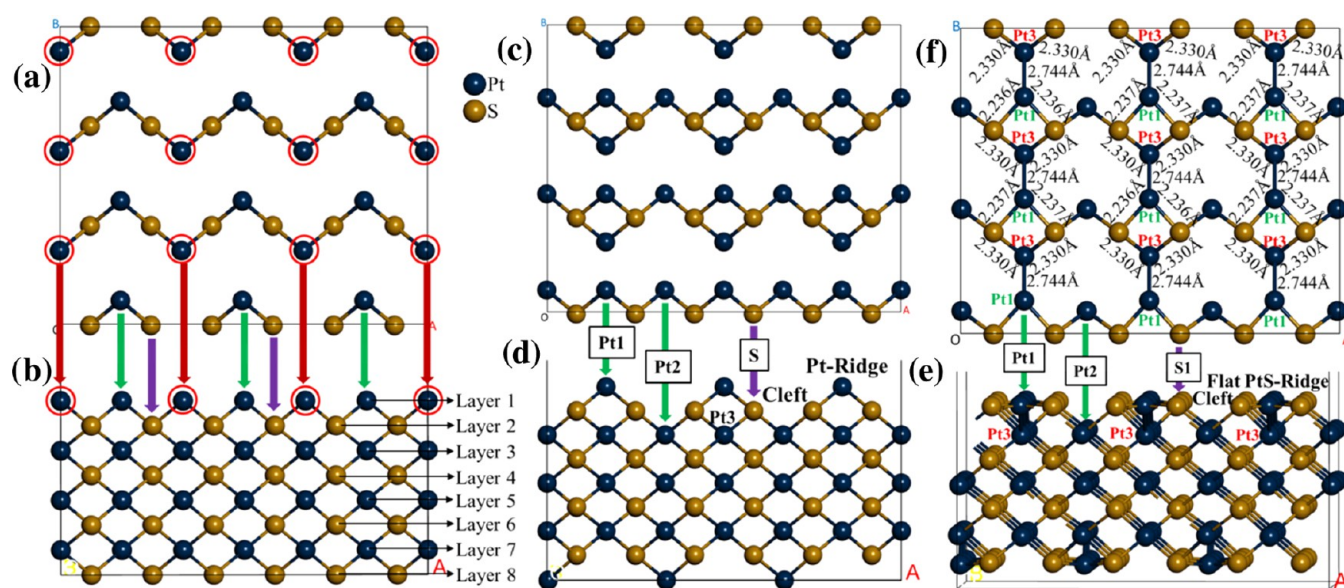


Figure 10. Pt-termination of the (001) surface: (a) view of unrelaxed unreconstructed top two layers, (b) unrelaxed unreconstructed side view, (c) view of unrelaxed reconstructed top three layers, (d) unrelaxed reconstructed side view, (e) relaxed reconstructed side view, and (f) view of relaxed reconstructed top three layers with bond lengths.

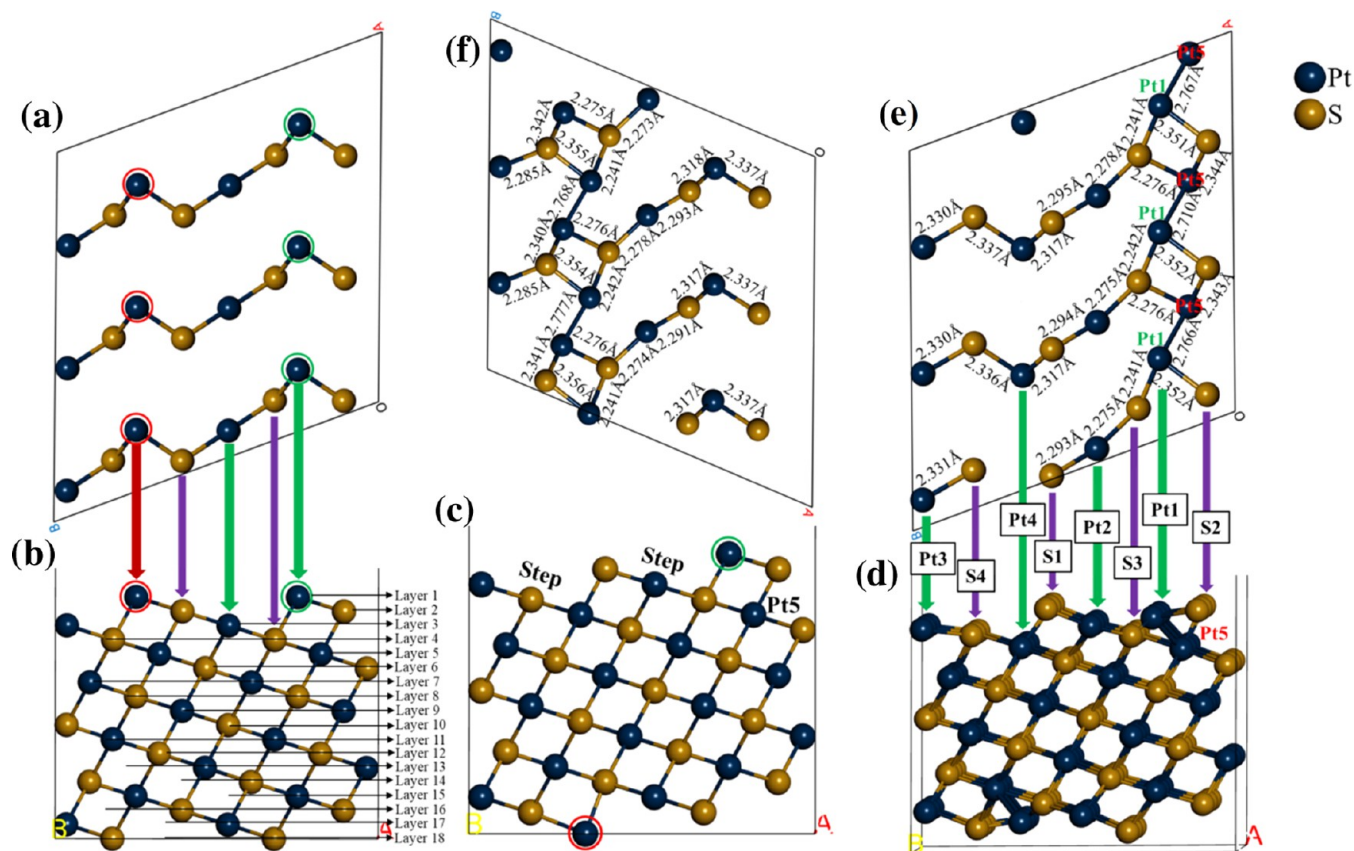


Figure 11. Pt-termination of the (111) surface: (a) view of unrelaxed unreconstructed top four layers, (b) unrelaxed unreconstructed side view, (c) unrelaxed reconstructed side view, (d) relaxed reconstructed side view, (e) view of relaxed reconstructed top five layers with bond lengths, and (f) view of relaxed reconstructed bottom five layers with bond lengths.

Table 4. Atomic Vertical Displacements (Δd_z , Å) of the Top Layers on Reconstructed (111) Surface Models, Obtained from the Unrelaxed ($d_{z(U)}$) and Relaxed ($d_{z(R)}$) Z-Atomic Positions^a

Rec-(111) surface						(211) surface		
Pt-termination			S-termination			S-termination		
layer	species	Δd_z	layer	species	Δd_z	layer	species	Δd_z
layer 1	Pt1	-0.0271	layer 1	S1	-0.0021	layer 1	S1	-0.0023
layer 2	S1	+0.0033	layer 2	Pt1	-0.0057	layer 2	Pt1	-0.0121
	S2	-0.0032		Pt2	-0.0215		Pt2	-0.0088
layer 3	Pt2	-0.0021	layer 3	S2	-0.0009	layer 3	S2	+0.0014
	Pt3	-0.0057		S3	+0.0020	layer 4	S3	+0.0019
layer 4	S3	-0.0013	layer 4	Pt3	-0.0011	layer 5	Pt3	-0.0013
	S4	+0.0011	layer 5	S4	-0.0010		Pt4	+0.0009
layer 5	Pt4	+0.0020	layer 6	Pt4	-0.0007	layer 6	S4	-0.0010
	Pt5	-0.0011						

^aNegative and positive values show inward and outward displacements, respectively.

shown in Figure 11c. Note that the unreconstructed Pt-Term surface has six Pt atoms in its first and third atomic layers and six S atoms in the second and fourth atomic layers, as shown in Figure 11a,b. The surface slab is fashioned with a stepped surface, where six Pt and three S atoms are exposed in each step, and its reconstruction creates a stepped surface that moves three Pt atoms to the bottom and exposes three S atoms in the fourth atomic layer. The relaxed reconstructed Pt-Term surface, as shown in Figure 11d, was noted to relax the Pt and S atoms in layers 1, 2, and 3 inward, except for S1 atoms in layer 2, which relaxed outward. The fourth atomic layer (layer 4) was composed of S3 and S4 atoms, and we noted that the

S3 atoms relaxed inward, while the S4 atoms relaxed outward. The fifth atomic layer (layer 5) resulted in Pt4 atoms relaxing outward, while Pt5 atoms relaxed inward, as displayed in Table 4 (also see Figure 11d for atom naming). The relaxed bond lengths of the top and bottom five exposed atomic layers are shown in Figure 11e,f, respectively. We observed that the Pt1 atoms in layer 1 circled in green relaxed inward, occupying an intermediate position between layers 2 and 3, and formed new Pt-Pt (Pt_2^{2+}) bonds with Pt atoms in layer 5 with lengths of 2.710, 2.766, and 2.767 Å for the top surface (Figure 11e).

Similar relaxation was observed at the bottom of the slab, resulting in Pt-Pt bonds with lengths of 2.777 and 2.768 Å

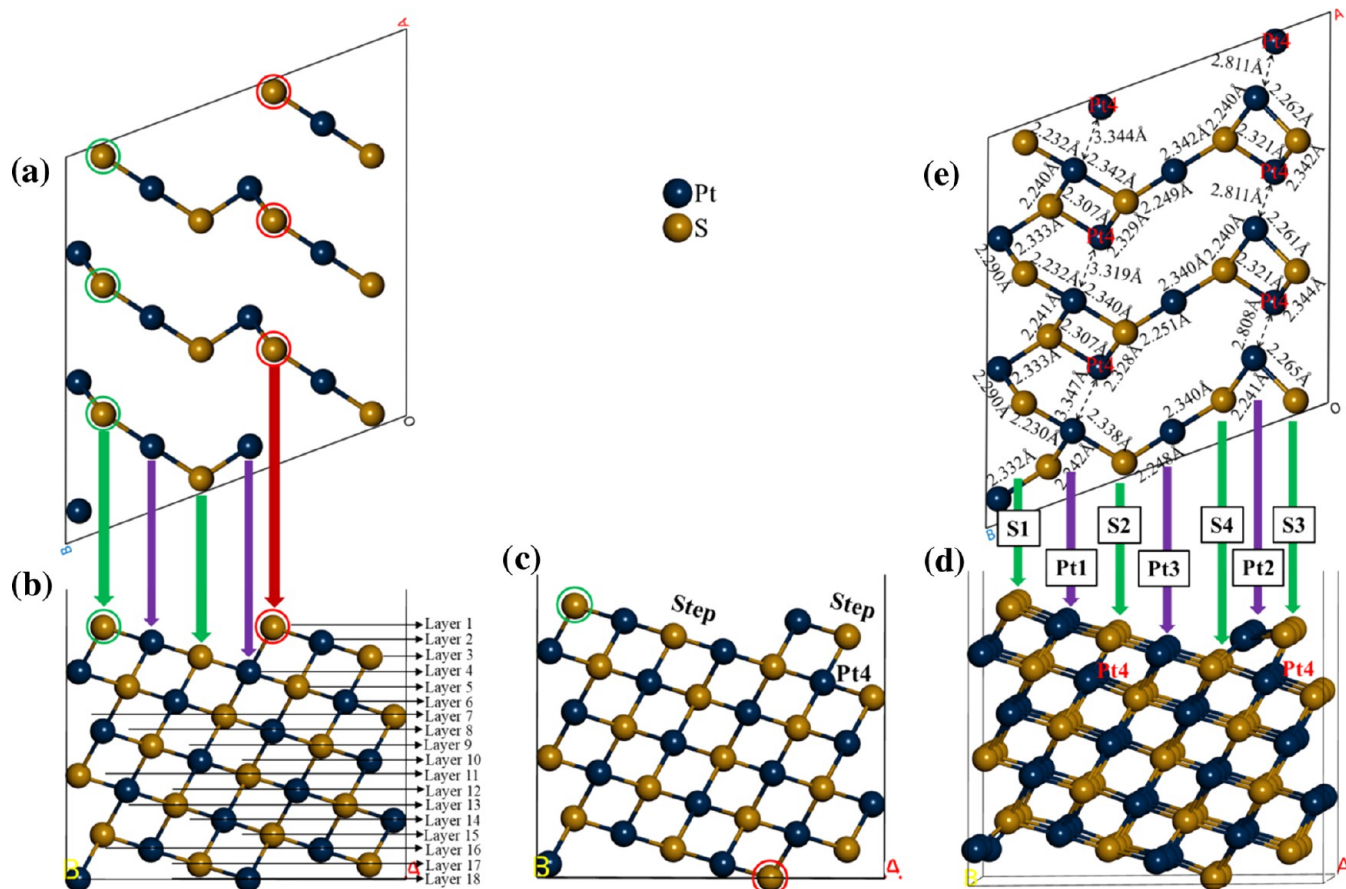


Figure 12. S-termination of the (111) surface: (a) view of unrelaxed unreconstructed top four layers, (b) unrelaxed unreconstructed side view, (c) unrelaxed reconstructed side view, (d) relaxed reconstructed side view, and (e) view of relaxed reconstructed top six layers with bond lengths.

(Figure 11f). These Pt–Pt bond lengths were larger than the Pt–Pt bond length of 2.700 Å determined from the sum of the atomic radii, suggesting weaker Pt–Pt bonds. We noted that on the unrelaxed reconstructed top Pt–Term surface, the Pt–S bond lengths were 2.320 Å on the top stepped surface, while on the relaxed surface, the bond lengths increased to 2.330/1, 2.337, 2.343/4, and 2.351/2 Å and decreased to 2.317 and 2.275/8 Å, as indicated in Figure 11e. These Pt–S bond lengths were shorter than the Pt–S bond length of 2.350 Å determined from the sum of the atomic radii, except for some, which were slightly larger. In Figure S11, we show the relaxed structure of the unreconstructed Pt–Term surface. We observed that the unreconstructed Pt–Term surface relaxes the Pt atoms inward. However, no new Pt–Pt bonds were formed. The relaxed Pt–S bond lengths decreased from 2.320 to 2.262 and 2.316 Å and increased to 2.335, 2.326, and 2.355 Å (see Figure S11c). These Pt–S bond lengths were shorter than the Pt–S bond length of 2.350 Å determined from the sum of the atomic radii, except for some, which were slightly larger.

We also carried out the reconstruction of S–Term by moving the top three S atoms circled in red (see Figure 12a,b) to the bottom of the slab to create a stoichiometric and symmetric surface slab, as shown in Figure 12c. The unreconstructed S–Term surface has six S atoms in layers 1 and 3 and six Pt atoms in layers 2 and 4, as shown in Figure 12a. The S–Term surface slab is also fashioned with a stepped surface, where six S and three Pt atoms are exposed in each step, and the reconstruction created a stepped surface that moved three S atoms to the bottom and exposed three Pt atoms in layer 4. The relaxed

reconstructed S–Term, as shown in Figure 12d, was noted to relax the Pt and S atoms in layers 1, 2, 4, 5, and 6 inward, while in the third atomic layer (layer 3), the S3 atoms relaxed outward and S2 atoms relaxed inward. The Pt2 atoms in layer 2 had the largest inward relaxation of -0.0215 Å, as displayed in Table 4. However, this large relaxation did not form new Pt–Pt bonds. The relaxed bond lengths of the top five exposed atomic layers are shown in Figure 12e. We noted that on the unrelaxed reconstructed S–Term surface, the Pt–S bonds were 2.320 Å on the top stepped surface, while on the relaxed stepped surface, the bond lengths decreased to between 2.230 and 2.318 Å and increased to between 2.321 and 2.344 Å, as shown in Figure 12e. Now, the relaxed structure of the unreconstructed S–Term, as shown in Figure S12, depicts similar relaxation as the reconstructed S–Term, where there was no surface self-reconstruction to form new Pt–Pt bonds (see Figure S12b). The Pt–S bond lengths were 2.320 Å on the unrelaxed top stepped surface, while on the relaxed stepped surface, the bond lengths decreased to 2.296, 2.302, and 2.319 Å, as shown in Figure S12c. It was clear that the reconstructed S–Term surface had decreased and increased Pt–S bond lengths, while the unreconstructed S–Term surface only had decreased Pt–S bond lengths, which suggested that the unreconstructed surface was more stable. All these Pt–S bond lengths were shorter than the Pt–S bond length of 2.350 Å determined from the sum of the atomic radii, which suggested Pt–S stable bonds.

3.7. (211) Surface (2 × 2) Supercell. The (211) surface has three terminations, two S–terminations (S–Term and S–

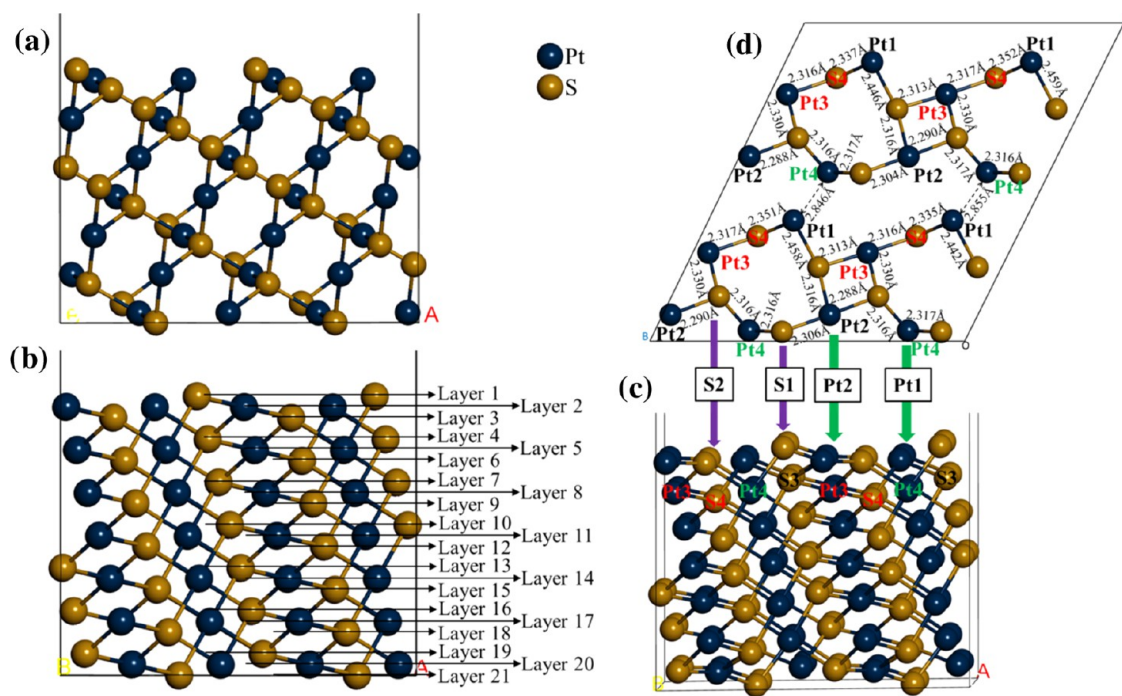


Figure 13. S-termination of the (211) surface: (a) unrelaxed OA vector side view, (b) unrelaxed OB vector side view, (c) relaxed OB vector side view, and (d) view of relaxed top six layers with bond lengths.

Term-A) and Pt-termination, which were modeled using a 2×2 supercell. We noted that the reconstruction of S-Term-A and Pt-Term would be similar, in which the reconstruction of S-Term-A would be performed by moving some top S atoms to the bottom of the slab, while the reconstruction of Pt-Term would be the opposite. Moreover, we found that S-Term did not require any reconstruction, since it was of Type II, a nondipole surface slab as described by Tasker.³² The nondipole symmetric S-Term of the (211) surface is composed of four S atoms in its first and third atomic layers and eight Pt atoms in the second atomic layer (Figure 13). The relaxation of S-Term displayed an inward relaxation of the Pt and S atoms on the top two layers (layers 1 and 2), Pt3 in layer 5 and S4 in layer 6, while S2 in layer 3, S3 in layer 4, and Pt4 in layer 5 relaxed outward, as shown in Table 4. We found that Pt1 relaxed inward largely by -0.0121 Å. We noted that the unrelaxed S-Term surface was composed of Pt–S bonds with a length of 2.320 Å, while on the relaxed surface, the bond lengths decreased to 2.288 , 2.290 , 2.306 , and $2.313/6/7$ Å and increased to 2.330 , 2.337 , $2.351/2$, 2.3442 , and 2.459 Å, as indicated in Figure 13d.

S-Term-A, as shown in Figure S13, has four S atoms in the first, second, and fourth atomic layers and eight Pt atoms in the third atomic layer. S-Term-A is the opposite flip top to bottom of the Pt-Term, they have similar orientations and their relaxations are similar. In this case (S-Term-A), the bottom of the slab formed new Pt–Pt bonds with lengths of 2.701 , 2.715 , and 2.734 Å (Figure S13e). These Pt–Pt bond lengths were larger than the Pt–Pt bond length of 2.700 Å determined from the sum of the atomic radii, suggesting weaker Pt–Pt bonds. As illustrated in Figure S13d, the Pt–S bond lengths changed from 2.320 to 2.330 , 2.308 , and 2.335 Å (see Figure S13d for other bond lengths). The Pt-Term of the (211) surface has eight Pt atoms in its first atomic layer, four S atoms in the second atomic layer, and four S atoms in the third atomic layer, as shown in Figure S14. After surface relaxation, we observed

an inward relaxation of the Pt atoms, which resulted in the formation of new Pt–Pt (Pt_2^{2+}) bonds with lengths of 2.659 , 2.707 , 2.702 , 2.744 , and 2.769 Å on the top surface, as shown in Figure S14. These Pt–Pt bond lengths were larger and shorter than the Pt–Pt bond length of 2.700 Å determined from the sum of the atomic radii, suggesting weaker and stronger Pt–Pt bonds, respectively. We noted that the Pt–S bonds on the top layers decreased from 2.320 to 2.314 , 2.310 , 2.296 , and 2.287 Å and increased to 2.328 , 2.345 , 2.358 , and 2.362 Å (see Figure S14d for other bond lengths). It is clear that all of the Pt–S bond lengths were shorter and larger than the Pt–S bond length of 2.350 Å determined from the sum of the atomic radii, which suggested weaker and stronger bond lengths, respectively.

4. DISCUSSION

We modeled and performed the reconstructions of different terminations of the low-Miller-index (001), (100), (101), (112), (110), (111), and (211) surfaces of cooperite (PtS). Based on the results presented in the previous sections, we can outline the different mechanisms of reconstruction. The (001) Pt-Term and S-Term, (100) PtS-Term and Pt-Term, (110) Pt-Term and S-Term, and (111) Pt-Term and S-Term surfaces were reconstructed, and their relaxation was described. We noted that the unreconstructed (001), (100), and (111) surfaces did not self-reconstruct, together with the nondipole symmetric (101) S-Term, (112) PtS-Term, and (211) S-Term surfaces. We observed that the unreconstructed (110) Pt-Term and S-Term, (101) Pt-Term and S-Term-B, and (211) Pt-Term and S-Term-A surfaces self-reconstructed, forming new Pt–Pt (Pt_2^{2+}) bonds. Among the reconstructed surfaces, we noted that only (110) Pt-Term and (111) Pt-Term surfaces relaxed and created new Pt–Pt bonds as they were described in the previous section. To understand these reconstruction mechanisms, it is important to reminisce that in the bulk, each S atom is coordinated with four Pt atoms in a tetrahedral

Table 5. Display the Unrelaxed (U) and Relaxed (R) Surface Energies, Percentage Relaxation, Top Layer Atom Coordination, Cell Parameters, Slab Chemical Formula, Number of Atoms, and Termination of the Cooperite (PtS) Surfaces

Termination	Surface slab models			Coordination		Cell parameters		Surface energies ($\text{J}\cdot\text{m}^{-2}$)		
	Cell	no. of atoms	Formula	Pt	S	<i>a</i>	<i>b</i>	($E_{\text{Surf}}^{\text{U}}$)	($E_{\text{Surf}}^{\text{R}}$)	Relaxation (%)
bulk		4	Pt ₂ S ₂	4	4	3.498	3.498			
				(001) surface						
Pt-term	(4 × 4)	128	Pt ₆₄ S ₆₄	2	4	13.990	13.990	2.417	2.300	4.84
S-term	(4 × 4)	128	Pt ₆₄ S ₆₄	4	2	13.990	13.990	2.461	2.300	6.54
Rec-Pt-term	(4 × 4)	128	Pt ₆₄ S ₆₄	2	3	13.990	13.990	2.446	2.270	7.20
Rec-S-term	(4 × 4)	128	Pt ₆₄ S ₆₄	3	2	13.990	13.990	2.760	2.662	3.55
				(100) surface						
PtS-term	(3 × 2)	96	Pt ₄₈ S ₄₈	4	3	10.493	12.191	1.904	1.816	4.62
Pt-term	(3 × 2)	96	Pt ₄₈ S ₄₈	2,4	4	10.493	12.191	1.884	1.804	4.25
Rec-PtS-term	(3 × 2)	96	Pt ₄₈ S ₄₈	3,4	3,4	10.493	12.191	1.713	1.632	4.73
Rec-Pt-term	(3 × 2)	96	Pt ₄₈ S ₄₈	2,4	3,4	10.493	12.191	1.877	1.793	4.48
				(101) surface						
Pt-term	(2 × 4)	128	Pt ₆₄ S ₆₄	2	4	14.055	13.990	2.615	2.289	12.47
S-term	(2 × 4)	128	Pt ₆₄ S ₆₄	3,4	3,4	14.055	13.990	1.448	1.381	4.63
S-term-B	(2 × 4)	128	Pt ₆₄ S ₆₄	4	1,3	14.055	13.990	2.587	2.298	12.64
				(112) surface						
PtS-term	(3 × 2)	120	Pt ₆₀ S ₆₀	3	3	14.839	15.699	1.723	1.633	5.22
				(110) surface						
Pt-term	(3 × 3)	144	Pt ₇₂ S ₇₂	2	4	18.286	14.839	2.169	1.930	11.02
S-term	(3 × 3)	144	Pt ₇₂ S ₇₂	4	2	18.286	14.839	2.161	1.953	9.63
Rec-Pt-term	(3 × 3)	144	Pt ₇₂ S ₇₂	2	3	18.286	14.839	2.215	1.912	13.68
Rec-S-term	(3 × 3)	144	Pt ₇₂ S ₇₂	3	2	18.286	14.839	2.298	2.132	7.22
				(111) surface						
Pt-term	(3 × 2)	108	Pt ₅₄ S ₅₄	2,3	3,4	14.934	14.156	1.900	1.787	5.95
S-term	(3 × 2)	108	Pt ₅₄ S ₅₄	3,4	2,3	14.934	14.156	1.900	1.789	5.84
Rec-Pt-term	(3 × 2)	108	Pt ₅₄ S ₅₄	2,3	2,3	14.934	14.156	2.051	1.779	13.26
Rec-S-term	(3 × 2)	108	Pt ₅₄ S ₅₄	2,3	2,3	14.934	14.156	2.050	1.878	8.39
				(211) surface						
S-term	(2 × 2)	112	Pt ₅₆ S ₅₆	2,3	2,3	15.641	14.055	1.820	1.671	8.19
S-term-A	(2 × 2)	112	Pt ₅₆ S ₅₆	3,4	2,3	15.641	14.055	1.821	1.670	8.29
Pt-term	(2 × 2)	112	Pt ₅₆ S ₅₆	2,3,4	2,3,4	15.641	14.055	1.822	1.653	9.28

geometry and each Pt atom forms coplanar bonds in coordination with four S atoms. During surface cleavage, the S and Pt atoms change their coordination, which is dependent on the surface termination cleavage, as shown in Table 5. Although the S atoms on the unreconstructed (110) Pt-Term and S-Term and (101) Pt-Term and S-Term-B surfaces lost two bonds, there was no formation of new S–S or Pt–S bonds. However, the Pt atoms on (110) Pt-Term and (111) Pt-Term surfaces lost two bonds, and due to their greater relaxation, they formed new Pt–Pt bonds to form a stable surface.

The relaxation of the surfaces and their reconstruction resulted in the stability of the surfaces as depicted in the surface energy calculations. Table 5 summarizes their surface energies before and after energy minimization. Before relaxation, the order of increasing surface energies, and therefore decreasing stability, was (101) > (211) > (100) > (112) > (111) > (110) > (001), which is different after relaxation, giving a decreasing stability order of (101) > (100) ≈ (112) > (211) > (111) > (110) > (001). Note that the order was established by taking into account only the most stable termination per surface (i.e., with the lowest surface energy), as these terminations would be most likely to cleave for each plane. Note that the asymmetric Pt-Term and S-Term-A of the (211) surface gave the lowest surface energy compared to the nondipole symmetric S-Term, which was attributed to the relaxation of the surfaces, forming new Pt–Pt bonds. However,

we considered the nondipole S-Term surface energy as this was an ideal stable surface. Table 5 displays the relaxation percentage of the surfaces, and we found that Rec-(110) Pt-Term had the largest relaxation among all surfaces with 13.68%, followed by Rec-(111) Pt-Term with 13.26%. These were attributed to their self-reconstruction, forming new Pt–Pt (Pt₂²⁺) bonds. The unreconstructed (001), (100), and (101) surfaces have the smallest relaxation of 3.55, 4.25, and 4.63%, respectively, which is attributed to their non-reconstruction after surface relaxation.

We noted that relaxation of the surfaces lowers the surface energies as seen from the change in unrelaxed to relaxed surfaces and therefore stabilizes the surfaces (Table 6). However, reconstruction of (001) S-Term, (110) S-Term, and (111) S-Term did not form stable surfaces (see Table 6). Furthermore, we observed that from the unrelaxed surfaces, the reconstruction of the surfaces gives lower surface energies, except for Rec-(001), Rec-(110), and Rec-(111), which depicts an increase in surface energies (Table 5).

Interestingly, it is clear that the relaxation of these reconstructed surface terminations produced lower surface energies and thus stable surfaces. However, for (001) S-Term, (110) S-Term, and (111) S-Term, the relaxed reconstructed surface gives higher surface energy compared to the relaxed unreconstructed surface. This is clearly depicted in Table 6, where their change in surface energies was positive. It is also

Table 6. Relaxed Surface Energies ($\text{J}\cdot\text{m}^{-2}$) for the Reconstructed ($E_{\text{Surf.}}^{\text{Rec.}}$) and Unreconstructed ($E_{\text{Surf.}}^{\text{Unrec.}}$) Surfaces, and the Reconstruction Surface Energy Change ($\Delta E_{\text{Surf.}}$)^a

Surface	Termination	$E_{\text{Surf.}}^{\text{Rec.}}$	$E_{\text{Surf.}}^{\text{Unrec.}}$	$\Delta E_{\text{Surf.}}$
(001)	Pt-term	2.270	2.300	-0.030
	S-term	2.662	2.300	+0.362
(100)	PtS-term	1.632	1.816	-0.184
	Pt-term	1.793	1.804	-0.011
(110)	Pt-term	1.913	1.930	-0.017
	S-term	2.132	1.953	+0.179
(111)	Pt-term	1.779	1.787	-0.008
	S-term	1.878	1.789	+0.089

^aNegative values indicate stable exothermic formation of the reconstructed surface, while positive values denote the opposite.

deduced in Table 6 that the other surfaces gave a negative surface energy change, thus producing more stability in the reconstructed surfaces. We noted that the (100) PtS-Term surface gave the lowest surface energy change ($-0.184 \text{ J}\cdot\text{m}^{-2}$), which suggests that the reconstruction was more stable among the reconstructed surfaces.

We constructed the Wulff⁵⁸ crystal morphology of cooperite using all of the lowest surface energies of the Miller index to identify the most preferred planes based on the appearance of the morphology. The morphology of cooperite crystals has been previously studied experimentally.⁸ Our calculated equilibrium morphology is expressed as an octahedron shape with truncated central corners, top point, and bottom point, as shown in Figure 14f. The morphology displays a number of planes, which indicated that the cooperite mineral has many surface cleavages. The multiple plane cleavage provides an explanation to the experimentally reported irregular crystal face appearance by Rozhdestvina et al.⁸ As expected, the (101) plane dominates the morphology, followed by the (001) surface that truncates the top and bottom points, while the (211) plane truncates the central corners of the octahedron. The (112) surface appears in a rectangle shape between the (101) and (011) planes. The (111), (110), and (100) surfaces do not appear in the morphology of cooperite due to the calculated relation between the energy of the surfaces and their position in the crystal. We calculated the ratios of the surfaces based on their morphological shapes, as shown in Figure 14f.

We observed that the (101), (112), (111), and (211) surfaces display similar octahedron shapes, as shown in Figure 14b–e, respectively. Furthermore, the (111) surface energy ratio to (101) $E_{\text{Surf.}(111)}/E_{\text{Surf.}(101)} = 1.29 < \sqrt{2}$; although the ratio is less than $\sqrt{2}$, the (111) surface is not expressed in the Wulff construction due to competition with the (101) surface. The ratio of the (100) surface to all surfaces is less than $\sqrt{2}$ due to its position in the crystal morphology, as shown in Figure 14a, where the (100) plane is on the sides of (001) morphology; thus, it is not expressed in the crystal morphology. In addition, the ratio of the (110) surface to all surfaces is less than $\sqrt{2}$ due to its position in the crystal morphology, as shown in Figure 14b, where the (110) plane is on the corners of (101) morphology; thus it is not expressed in the crystal morphology (Figure 14f) due to competition with the (211) surface, which truncates the corners, as shown in Figure 14f. There are many ways to modify the shape of nanoparticles, such as solvents, media, capping agents, temperature, or viscosity.⁵⁵ However, the Wulff morphology shown in Figure 14f expresses a particle produced under conditions of perfect thermodynamic equilibrium, vacuum, and at 0 K. The computational predicted cooperite equilibrium morphology, as shown in Figure 14f, is in agreement with the reported irregular shapes of cooperite morphology by Rozhdestvina et al.⁸ and experimental XRD patterns.^{9–11} In addition our results showed a preferential cleavage of the (101) or (011) surface, which was reported to have a larger interplanar distance from the electron diffraction pattern by Rozhdestvina et al.⁸ This confirms that minerals prefer to cleave along the larger interplanar distance with few interplanar bonds; hence, the (101) plane is the most dominant plane. We, therefore, establish that XRD is a viable tool to predict the most stable surface even prior to surface studies. This is because the powder of the mineral used in the XRD is dominated by the most preferred cleavage of that mineral, and therefore, the radiation source would reflect strongly on those surfaces, resulting in high intensities.

We computed the band structures for the relaxed most stable surfaces before and after reconstruction, and those of nondipole surfaces, as shown in Section S14 in the Supporting Information, to obtain their band gap that can be related to their chemical reactivity stability, as depicted in Table 7. The band gap is related to the highest occupied molecular orbital (HOMO) and lowest unoccupied molecular orbital (LUMO) gap of molecules, where it has been reported that the molecule

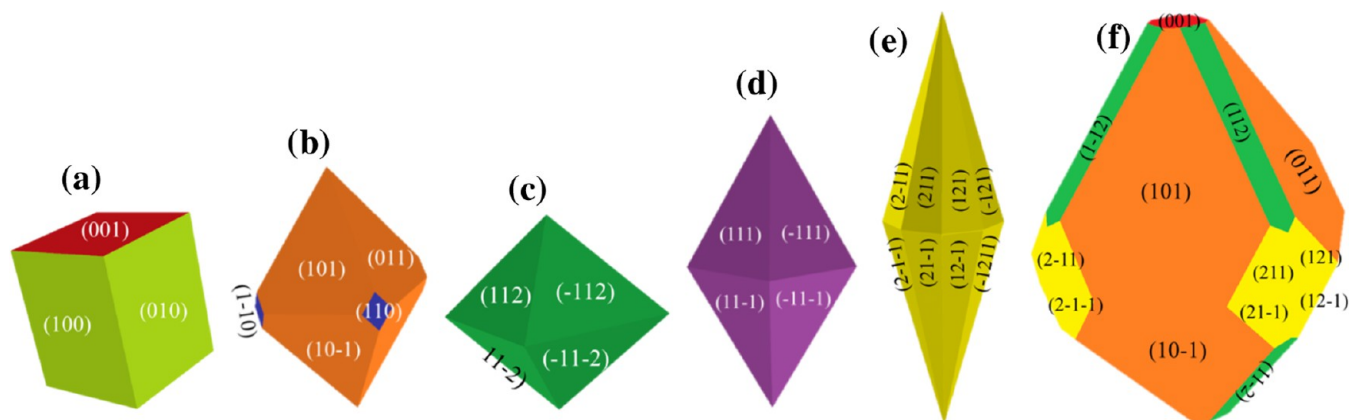


Figure 14. Cooperite crystal morphology shapes: (a) (001) and (100), (b) (101) and (110), (c) (112), (d) (111), and (e) (211) morphology shapes and (f) Wulff equilibrium morphology.

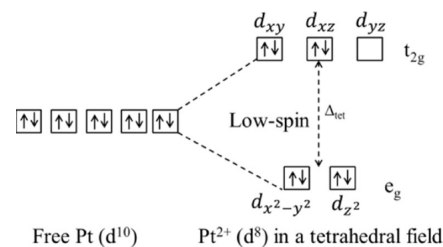
Table 7. Band Structure Band Gaps for the Relaxed Reconstructed and Unreconstructed Surfaces

Surface model	Band gap (eV)
PtS bulk	1.408
(001) Pt-Term	0.319
Rec-(001) Pt-Term	0.521
(100) PtS-Term	0.372
Rec-(100) PtS-Term	0.702
(110) Pt-Term	0.437
Rec-(110) Pt-Term	1.090
(101) S-Term	1.202
(111) Pt-Term	0.511
Rec-(111) Pt-Term	0.559
(112) PtS-Term	1.219
(211) S-Term	0.784
(211) Pt-Term	0.337

with the lowest HOMO–LUMO gap has higher reactivity, while the molecule with the highest HOMO–LUMO gap is less reactive.^{61,62} We used this theory to describe the surface chemical reactivity stability using the band gaps, where a higher band gap depicts less reactivity and thus a more chemical stable surface. It is paramount to remember that a stable surface has the lowest surface energy, which implies a less reactive surface. From Table 7, we found that the order of decreasing band gaps, and therefore decreasing chemical stability based on reconstructed and nondipole surfaces, is (112) > (101) > (110) > (211) > (100) > (111) > (001), which depicts that the Rec-(112) PtS-Term surface is more chemically stable among all of the surfaces. It is interesting to note that the band gap chemical stability order is different from the surface energy stability order (i.e., (101) > (100) \approx (112) > (211) > (111) > (110) > (001)). This may suggest that although the (101) and (100) surfaces have lower surface energies than the (112) surface, which depicts preferential surface cleavage, the chemical behavior of the (112) surface is more stable. This may be ascribed to the bonding character of the (112) surface, since we observed that PtS-termination has all Pt and S atoms on top of the three-coordinated surface. Although the (101) S-Term surface has similar coordination, it is slightly more reactive than the (112) surface. Furthermore, we noted that the reconstructed surfaces increase the band gap from the unreconstructed surfaces, suggesting stability. Note

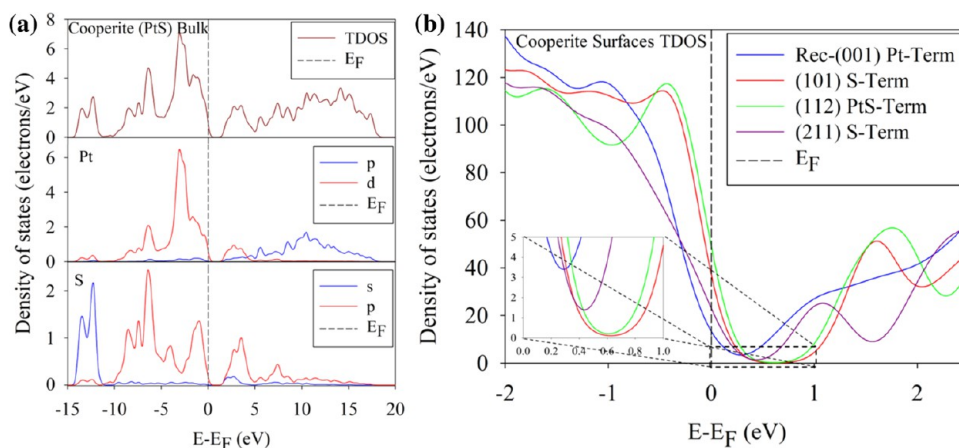
that although the (211) Pt-Term surface had lower surface energy than the (211) S-Term surface, the band gap of the (211) Pt-Term surface is lower than that of the (211) S-Term surface, suggesting that the (211) S-Term surface is more chemically stable (see Table 7). Moreover, we found that all reconstructed and nondipole surfaces have lower band gaps than the cooperite bulk model band gap (1.408 eV), which shows that the bulk is less reactive than the surfaces (Table 7).

In Figure 15a, we show the density of states (DOS) for the cooperite bulk model, which includes the partial density of states (PDOS) for the Pt and S atoms. In the cooperite bulk models, the sulfur and platinum atoms have oxidation numbers of -2 and $+2$, respectively. The valence electronic configuration of uncoordinated (free) Pt is $5d^96s^1$ or $5d^{10}(e_g)^4(t_{2g})^6$ and that of uncoordinated (free) S is $3s^2p^4$. Since Pt is tetrahedrally coordinated by four S atoms, the d-orbital splits into two (e_g) and three (t_{2g}) states, where the e_g states are lower in energy than the t_{2g} states due to the tetrahedral field from the S atoms. Since the S atoms impose a low-spin on Pt atoms, the Pt d-orbital splitting is occupied in the form of Pt^{2+} : $(e_g)^4(t_{2g})^4$, as also shown in Scheme 1. The low-spin results in

Scheme 1. Pt Atom d-Orbitals in Tetrahedral Field Splitting

no unpaired electrons, and the spin-up and spin-down are equally occupied, suggesting a nonmagnetic behavior. The total density of states (TDOS) in Figure 15a shows semiconductor behavior with a band gap of 1.408 eV, as determined by the band structure (Figure S1), located at the conduction band (CB), just above the Fermi energy (E_F).

Now, we compare the stable surfaces as they appear on the Wulff crystal morphology from TDOS, as shown in Figure 15b. It is clear that Rec-(001) Pt-Term has the lowest DOS at E_F . However, based on the band gap formations, the trend

**Figure 15.** Cooperite density of states: (a) density of states of the bulk cooperite model and (b) total density of states of cooperite stable surfaces as they appear on crystal morphology.

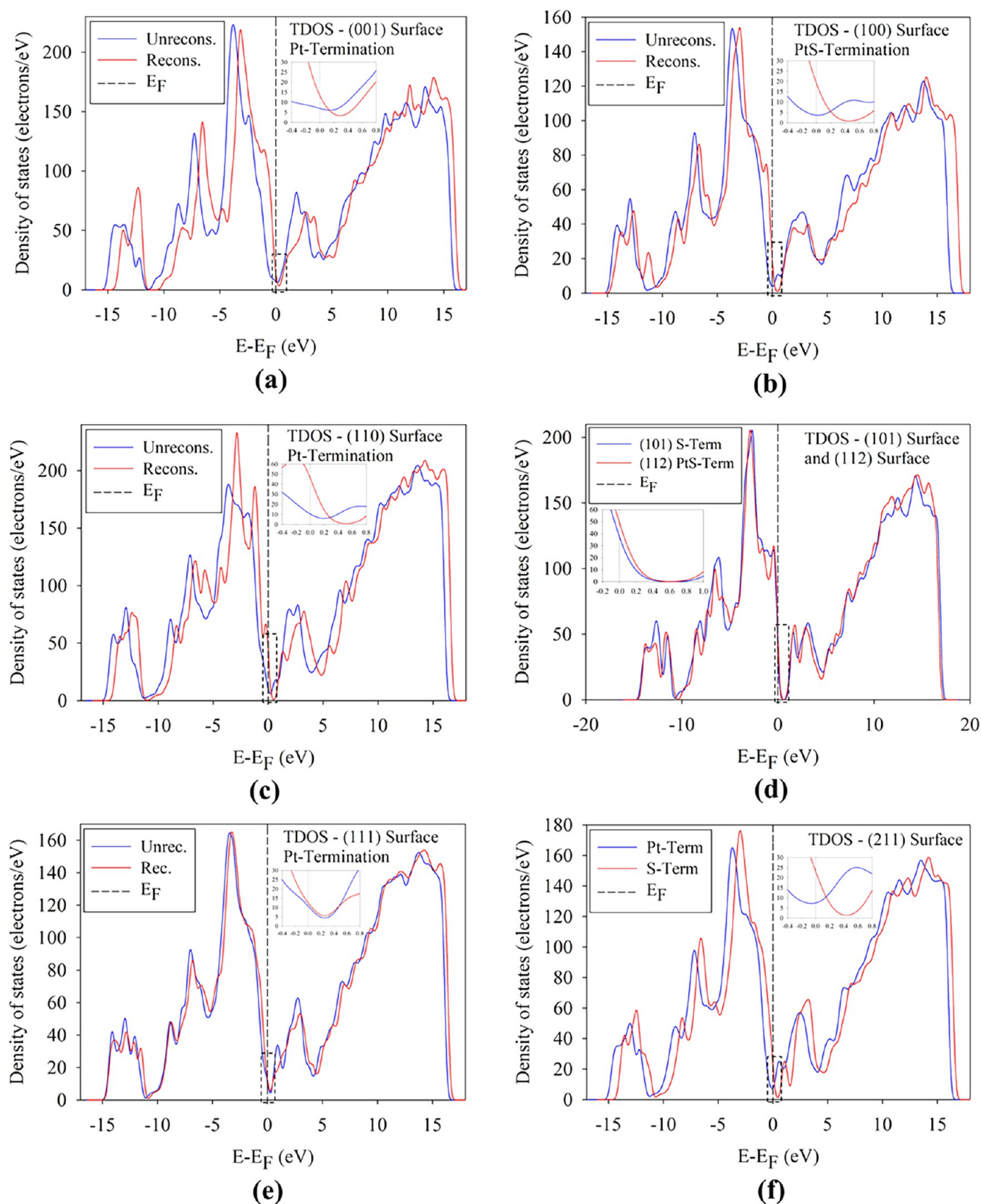


Figure 16. Total density of states (TDOS) for cooperite surfaces: (a) Pt-termination (001) unreconstructed and reconstructed surfaces TDOS, (b) PtS-termination (100) unreconstructed and reconstructed surfaces TDOS, (c) Pt-termination (110) unreconstructed and reconstructed surfaces TDOS, (d) S-termination (101) surface and PtS-termination (112) surface TDOS, (e) Pt-termination (111) unreconstructed and reconstructed surfaces TDOS, and (f). (211) surface S-termination and Pt-termination TDOS.

Table 8. Calculated Mulliken Population Atomic Charges for the Bulk and Relaxed Stable Surface Terminations

Atoms	Populations atomic charges e^-					
	PtS bulk	Rec-(001) Pt-Term	(112) PtS-Term			
Pt	+0.13 e^-	+0.03 e^-	+0.20 e^-			
S	-0.13 e^-	-0.13 e^-	-0.29 e^-			
			PtS surfaces			
	Rec-(100) PtS-Term	Rec-(110) Pt-Term	(101) S-Term	Rec-(111) Pt-Term	(211) S-Term	
Pt1	+0.24 e^-	+0.25 e^-	+0.18 e^-	+0.17 e^-	+0.25 e^-	
Pt2	+0.13 e^-	+0.17 e^-	+0.14 e^-	+0.09 e^-	+0.14 e^-	
Pt3	+0.13 e^-	-0.02 e^-		+0.22 e^-	+0.18 e^-	
Pt4				+0.16 e^-	+0.03 e^-	
Pt5				+0.06 e^-		
S1	-0.24 e^-	-0.13 e^-	-0.24 e^-	-0.08 e^-	-0.08 e^-	
S2	-0.18 e^-		-0.19 e^-	-0.23 e^-	-0.24 e^-	
S3				-0.07 e^-	-0.15 e^-	
S4				-0.30 e^-	-0.16 e^-	

changes, depicting (101) S-Term with lower DOS and suggesting stability. This indicated that in this case, the electronic stability is determined by the band gap of the surfaces. It is clear that the (101) and (112) surfaces have similar electronic behavior, as also found from the band gaps in Table 7.

Therefore it is clearly eminent that there is chemical stability competition between the (101) S-Term and (112) PtS-Term surfaces, since the (101) S-Term surface has slightly lower DOS than the (112) PtS-Term surface at around 0.6 eV, just above E_F . In Figure 16, we found that all reconstructed surfaces display a higher DOS at E_F compared to their corresponding unreconstructed surfaces. However, we noted that between 0.2 and 0.8 eV (band gaps region), the reconstructed surfaces have lower DOS. This suggests that the band gap is the determining factor for the reactivity stability of the surfaces (Figure 16a–c,e). It is clear from the band gaps shown in Table 7 that the reconstructed surfaces are more chemically stable. Similar behavior was noted for (211) S-Term and Pt-Term, where S-Term is electronically stable based on the band gap (Figure 16f). Although the (112) PtS-Term surface appears small on the edges of the crystal morphology, owing to its stable chemical reactivity stability based on its band gap and DOS, it should be considered during surface adsorption. This behavior is in correlation with our computational XRD and reported experimental XRD¹¹ patterns, where the (112) peak is the second highest peak, which depicts an important feature of cooperite; thus, the (112) and (101) surfaces are of paramount importance for future studies.

The Mulliken population atomic charges were computed for the top-exposed atomic layers to examine the change in charges on the surfaces in comparison to the bulk model, as shown in Table 8. We found that the bulk model with four-coordinated Pt and S atoms possessed charges of Pt = +0.13 e^- and S = -0.13 e^- , which indicated that the bulk model was charge neutral, i.e., +0.13 e^- + (-0.13 e^-) = 0 e^- . In the case of the surfaces, we noted that the Rec-(001) Pt-Term surface possessed charges of Pt = +0.03 e^- and S = -0.13 e^- , as shown in Table 8. Note that on this surface, the Pt atoms were two-coordinated, while the S atoms were three-coordinated. Although the S atoms were less coordinated compared to the bulk, they possessed the same charges as the four-coordinated S atoms in the bulk model. However, the Pt atom charges were less positive, which suggested electron loss from the bulk to the surfaces. This further suggested that the Pt atoms were more

reactive than the S atoms. In the case of the Rec-(100) PtS-Term surface, we found that the four-coordinated Pt1 atoms and three-coordinated S1 atoms on the PtS-Ridge possessed charges of +0.24 e^- and -0.24 e^- , as shown in Table 8, respectively. This suggested that the PtS-Ridge was charge neutral, while the three-coordinated Pt2 and four-coordinated Pt3 atoms at the Cleft sides still possessed the same charges as the bulk model. The four-coordinated S2 atoms at the Cleft floor possessed a charge of -0.18 e^- , and since the charges were more negative, it was suggested that the S2 atoms gained charges. The (101) S-Term surface was terminated by Pt and S atoms, which were three- and four-coordinated, respectively. We found that the three-coordinated Pt2 atoms and four-coordinated Pt1 atoms possessed +0.14 e^- and +0.18 e^- charges (Table 8), respectively, which suggested that the Pt2 atoms would be more reactive than the Pt1 atoms, since they possessed less positive charges. Similar behavior would be expected for three-coordinated S1 atoms, which would be more reactive, since they possessed more negative charges (-0.24 e^-) compared to the four-coordinated S2 atoms (-0.19 e^-). The (112) PtS-Term surfaces possessed charges of Pt = +0.20 e^- and S = -0.29 e^- , which were both three-coordinated, as shown in Table 8. Since the Pt atoms adopt more positive charges, while the S atoms adopt more negative charges, it is suggested that the Pt atoms lose charges to the S atoms. By comparing (101) S-Term surface reactivity to (112) PtS-Term surface reactivity, it is found that the (101) surface is more reactive than the (112) surface due to the Pt atoms possessing less positive charges than the Pt atoms on the (112) surface. In addition, the S atoms on the (112) surface are also more reactive than those on the (101) surface due to more negative charges. This behavior has been found from the band structure band gaps, where the (112) surface has a larger band gap compared to the (101) surface, suggesting chemical stability (i.e., less reactive).

In the case of the Rec-(110) Pt-Term surface, we found that the three-coordinated Pt1 atoms possessed +0.25 e^- charges, while the three-coordinated S1 atoms possessed -0.13 e^- charges, as shown in Table 8. The four-coordinated Pt2 atoms were found to adopt more positive charges (+0.17 e^-) than the bulk model. Interestingly, we observed that the five-coordinated Pt3 atoms adopted a negative charge of -0.02 e^- . Note that Pt1 and Pt3 were three- and five-coordinated due to the new Pt–Pt bond formation, respectively. It was clear that Pt1 atoms lost charges, while Pt3 atoms gained charges, which

was attributed to the new Pt–Pt bond formation between Pt1 and Pt3, which resulted in charge transfer from Pt1 to Pt3. The Rec-(111) Pt-Term has similar new Pt–Pt bond formation on the surface, which resulted in three-coordinated Pt1 atoms and five-coordinated Pt5 atoms. These Pt atoms were found to possess charges of $Pt1 = +0.17e^-$ and $Pt5 = +0.06e^-$ (Table 8), and it was clear that Pt1 adopted more positive charges, while Pt5 adopted less positive charges, which indicated charge loss and gain, respectively. An examination of the (111) Pt-Term surface, which was a stepped surface, depicted a number of exposed atoms on the surface. As shown in Table 8, after analyzing this surface, we found that the three-coordinated Pt2 atoms were coordinated to surface S1 and S3 atoms (S1–Pt2–S3). We noted that Pt2 possessed $+0.09e^-$ and gained charges, while S1 ($-0.08e^-$) and S3 ($-0.07e^-$) lost charges and suggested a charge transfer to the Pt2 atoms. The three-coordinated Pt3 atoms were coordinated to the surface S2 and S4 atoms (S2–Pt3–S4). We found that Pt3 adopted a more positive charge of $+0.22e^-$ (charge loss), while S2 ($-0.23e^-$) and S4 ($-0.30e^-$) gained charges, which suggested that Pt3 atoms lost charges to the S2 and S4 atoms. On the other hand, the four-coordinated Pt4 atoms ($+0.16e^-$) lost charges and were coordinated to S1 and S4 atoms, which suggested that S4 atoms gained charges from Pt4 and Pt3, while S1 atoms lost charges to Pt2. This suggested that Pt2 atoms would be more reactive among the Pt atoms on the (111) Pt-Term surface due to less positive charges ($+0.09e^-$). By analyzing the (211) S-Term surface, we found that the two-coordinated Pt1 atoms adopt more positive charges ($+0.25e^-$), while the three-coordinated Pt2 atoms possessed a charge of $+0.14e^-$ (see Table 8). It was clear that Pt1 atoms lost greater charges. The two-coordinated S1 atoms possessed a charge of $-0.08e^-$, while the three-coordinated S2 atoms possessed a charge of $-0.24e^-$, which showed that S1 lost charges, while S2 gained charges. We found that Pt4 gained charges and was coordinated to S1 and S2, which demonstrated that S1 lost charges to Pt4 atoms. These atomic charges depicted that the surfaces would have different reactivities, which would be largely dependent on the atomic coordination and possessed the charge state.

5. CONCLUSIONS

The study utilized the computational method of density functional theory with dispersion correction (TS) and the *U* parameter (DFT-D+*U*) to investigate the reconstruction of the (001), (100), (101), (112), (110), (111), and (211) cooperite (PtS) surfaces. The (001), (100), (110), and (111) cleavages had two possible terminations, i.e., Pt-Term and S-Term for (001), (110), and (111) and PtS-Term and Pt-Term for (100), while (101) cleaved along three terminations (Pt-Term, S-Term (nondipole), and S-Term-B), and (211) also cleaved along three terminations (S-Term (nondipole), S-Term-A, and Pt-Term). The (112) surface only had one nondipole PtS-termination. The reconstructions of (001), (100), (110), and (111) surfaces were investigated in detail. From the structural analyses of these 15 surfaces, one major relaxation mechanism emerged for the cooperite surfaces. It was established that the relaxation of the reconstructed Pt-Term of (110) and (111) surfaces, resulted in self-reconstruct, whereby the Pt^{2+} cation formed new Pt–Pt (Pt_2^{2+}) bonds on the top and bottom of the surfaces. In addition, the unreconstructed (101) Pt-Term and S-Term, (110) Pt-Term and S-Term-B, and (211) Pt-Term and S-Term-B also formed new Pt–Pt (Pt_2^{2+}) bonds, where for

Pt-Term, it occurred on top, while for S-Term, S-Term-A, and S-Term-B, it occurred at the bottom of the surfaces. In the case of unreconstructed and reconstructed (001) Pt-Term and S-Term, (100) PtS and S-Term, nondipole (101) S-Term, nondipole (112) PtS-Term, (111) S-Term, and nondipole (211) S-Term surfaces, no new bond formation was observed, we only depicted inward and outward relaxation of the Pt and S atoms. Similar behavior was depicted for the unreconstructed (111) Pt-Term surface.

The calculated surface free energies of (001), (100), (101), (112), (110), (111), and (211) cooperite surfaces of stoichiometric planes indicated the order of decreasing stability as $(101) > (100) \approx (112) > (211) > (111) > (110) > (001)$, after relaxation. This indicated that the most stable surface is the (101) S-Term and dominated the crystal morphology. However, the Rec-(001) Pt-Term, (112) PtS-Term, and (211) S-Term also appeared on the crystal morphology, leading to an octahedron shape with truncated corners under equilibrium conditions. Despite the Rec-(100) PtS-Term surface having the surface energy of the same order of magnitude as the others and being slightly more stable than the (112) PtS-Term and (211) S-Term surfaces, it was not expressed in the Wulff construction due to competition with the Rec-(001) Pt-Term surface. The structural and electronic properties of the reconstructed and nondipole surfaces were discussed in detail. We noted that the reconstructed surfaces increased the band gap compared to the unreconstructed surfaces, suggesting stability. From the total density of states, we also observed that the Rec-(001) Pt-Term surface had lower DOS at E_F among all surfaces. However, when the band gap forms, the (101) S-Term surface had low DOS followed by the (112) PtS-Term surface. We gathered from the band structure band gap that the chemical behavior of the (112) PtS-Term surface was more stable, suggesting competing chemical stability between (112) PtS-Term and (101) S-Term surfaces. These electronic properties demonstrated that the stability and chemical reactivity of these surfaces would be determined by the band gaps. Furthermore, the calculated Mulliken population atomic charges demonstrated that the surfaces had different reactivities, which would largely be dependent on the atomic coordination and charge state.

Our results indicated that the cleavage of the cooperite surfaces led to reconstruction of the surfaces, resulting in Pt–Pt bond formation. Although the (112) PtS-Term plane appears small relative to the (101) S-Term plane on the morphology, it is of interest for adsorption due to its chemical reactivity stability based on the band gap and DOS. The computed Wulff crystal morphology and XRD were in agreement with the experimental formation of irregular morphology shapes and XRD pattern findings, respectively. We, therefore, established that the XRD was a viable tool to predict the most stable surface even prior to surface studies. These results suggested that during froth flotation, the (101), (001), (112), and (211) surfaces as determined by the surface morphology would be present and largely dominated by the (101) surface in the crushed cooperite mineral. Therefore these surfaces would play a crucial role in interactions with reagents such as collectors or depressants.

■ ASSOCIATED CONTENT


Supporting Information

The Supporting Information is available free of charge at <https://pubs.acs.org/doi/10.1021/acsomega.2c02867>.

Figure of the cooperite band structure; figures for surface cleavage and different terminations; figures for unreconstructed surfaces; and plots for surface band structures (PDF)

AUTHOR INFORMATION

Corresponding Author

Peace P. Mkhonto – Materials Modelling Centre, University of Limpopo, Sovenga 0727, South Africa;  orcid.org/0000-0001-5091-3658; Email: peace.mkhonto@ul.ac.za

Author

Phuti E. Ngoepe – Materials Modelling Centre, University of Limpopo, Sovenga 0727, South Africa

Complete contact information is available at:

<https://pubs.acs.org/10.1021/acsomega.2c02867>

Notes

The authors declare no competing financial interest.

ACKNOWLEDGMENTS

This work was performed at the Materials Modelling Centre at the University of Limpopo. The authors acknowledge the financial support received from the Department of Science and Innovation (DSI) and the National Research Foundation (NRF) of South Africa. The authors also greatly acknowledge the Centre for High-Performance Computing (CHPC) for supercomputing resources.

REFERENCES

- O'Connor, C. T.; Shackleton, N. J. Investigations into the Recovery of Platinum Group Minerals from the Platreef Ore of the Bushveld Complex of South Africa. *Platinum Met. Rev.* **2013**, *57*, 302–309.
- Merkle, R. K. W.; Verryin, S. M. C. Cooperite and Braggite from the Bushveld Complex: Implications for the Miscibility Gap and Identification. *Miner. Deposita* **2003**, *38*, 381–388.
- Cooper, R. A. A New Platinum Mineral in the Rustenburg Norites. *J. Chem. Metall. Mineral. Soc. South Africa* **1928**, *28*, 281–283.
- Bannister, F. A. Determination of Minerals in Platinum Concentrates from the Transvaal by X-ray Methods. *Mineral. Mag.* **1932**, *23*, 188–206.
- Maier, W. D.; Barnes, S. -J.; Groves, D. I. The Bushveld Complex, South Africa: Formation of Platinum–Palladium, Chrome- and Vanadium-Rich Layers via Hydrodynamic Sorting of a Mobilized Cumulate Slurry in a Large, Relatively Slowlycooling, Subsiding Magma Chamber. *Miner. Deposit* **2013**, *48*, 1–56.
- Schouwstra, R. P.; Kinloch, E. D. A Short Geological Review of the Bushveld Complex. *Platinum Met. Rev.* **2000**, *44*, 33–39.
- Criddle, A. J.; Stanley, C. J. Characteristic Optical Data for Cooperite, Braggite, and Vysotskit. *Can. Mineral.* **1985**, *23*, 149–162.
- Rozhdestvina, V. I.; Udovenko, A. A.; Rubanov, S. V.; Mudrovskaya, N. V. Structural Investigation of Cooperite (PtS) Crystals. *Crystallogr. Rep.* **2016**, *61*, 193–202.
- Bannister, F. A. Determination of Minerals in Platinum Concentrates from the Transvaal by X-ray Methods. *Mineral. Mag. J. Mineral. Soc.* **1932**, *23*, 188–206.
- Cabri, L. J.; Laflamme, J. H. G.; Stewart, J. M. On Cooperite, Braggite, and Vysotskite. *Am. Mineral.* **1978**, *63*, 832–839.
- Rozhdestvina, V. I.; Ivanov, A. V.; Zarembo, M. A.; Antsutkin, O. N.; Forsling, W. Single-crystalline Cooperite (PtS): Crystal-chemical Characterization, ESR Spectroscopy, and ¹⁹⁵Pt NMR Spectroscopy. *Crystallogr. Rep.* **2008**, *53*, 391–397.
- Mkhonto, D.; Ngoepe, P. E.; Cooper, T. G.; de Leeuw, N. H. A Computer Modelling Study of the Interaction of Organic Adsorbates with Fluorapatite Surfaces. *Phys. Chem. Miner.* **2006**, *33*, 314–331.
- Ntoahae, P. S. Application of Computer Simulation Methods to the Study of Platinum Group Minerals. Ph.D. Thesis, University of Limpopo: Polokwane, Limpopo Province, South Africa, 2005.
- Masenyana, M. A. Computational Modelling Studies of Precious Mixed Metals Sulphides. M.Sc. Dissertation, University of Limpopo: Polokwane, Limpopo Province, South Africa, 2016.
- Hung, A.; Yarovskiy, I.; Russo, S. P. Density Functional Theory Studies of Xanthate Adsorption on the Pyrite FeS₂ (110) and (111) Surfaces. *J. Chem. Phys.* **2003**, *118*, 6022–6029.
- Stirling, A.; Bernasconi, M.; Parrinello, M. J. Ab Initio Simulation of H₂SH₂S Adsorption on the (100) Surface of Pyrite. *Chem. Phys.* **2003**, *119*, 4934–4939.
- Chen, V. H. -Y.; Mallia, G.; Martinez-Casado, R.; Harrison, N. M. The Surface Morphology of CuFeS₂: the Stability of the Polar (112)/(112) Surface Pair. *Phys. Rev. B* **2015**, *92*, 1–9.
- Mkhonto, P. P.; Zhang, X.; Lu, L.; Zhu, Y.; Han, L.; Ngoepe, P. E. Unravelling the Performance of Oxycarbonyl-Thiocarbamate Collectors on Chalcopyrite using First-Principles Calculations and Micro-Flotation Recoveries. *Appl. Surf. Sci.* **2021**, *563*, 150332.
- Waterson, C. N.; Sindt, J. O.; Cheng, J.; Tasker, P. A.; Morrison, C. A. First-Principles Study on Ligand Binding and Positional Disorder in Pentlandite. *J. Phys. Chem. C* **2015**, *119*, 25457–25468.
- Lu, L.; Yu, S. Metal Distribution in Iron-Nickel Sulfide Mineral Pentlandite: First-Principles Study. *Chem. Phys. Lett.* **2019**, *736*, 136786.
- Mkhonto, P. P.; Chauke, H. R.; Ngoepe, P. E. In *The Effect of Thiol Collectors on Nickel-rich (110) Pentlandite Surface Using Density Functional Theory*, Proceedings of SAIP2017, 2018; pp 95–100.
- Waterson, C. N.; Tasker, P. A.; Farinato, R.; Nagaraj, D. R.; Shackleton, N.; Morrison, C. A. A Computational and Experimental Study on the Binding of Dithio Ligands to Sperrylite, Pentlandite, and Platinum. *J. Phys. Chem. C* **2016**, *120*, 22476–22488.
- Nemutudi, B.; Mkhonto, P. P.; Ngoepe, P. E. Oxidation Behaviour of Sperrylite and Platarsite (100) Surfaces: A DFT study. *Mater. Today Commun.* **2022**, *32*, 103868.
- Hung, A.; Muscat, J.; Yarovskiy, I.; Russo, S. P. Density Functional Theory Studies of Pyrite FeS₂ (111) and (210) Surfaces. *Surf. Sci.* **2002**, *520*, 111–119.
- de Oliveira, C.; Lima, G. F.; Abreu, H. A.; Duarte, H. A. Reconstruction of the Chalcopyrite Surfaces: A DFT Study. *J. Phys. Chem. C* **2012**, *116*, 6357–6366.
- Klauber, C. Fracture-Induced Reconstruction of a Chalcopyrite (CuFeS₂) Surface. *Surf. Interface Anal.* **2003**, *35*, 770.
- Wei, Z.; Li, Y.; Gao, H.; Zhu, Y.; Qian, G.; Yao, J. New Insights into the Surface Relaxation and Oxidation of Chalcopyrite Exposed to O₂ and H₂O: A First-Principles DFT Study. *Appl. Surf. Sci.* **2019**, *492*, 89–98.
- Mkhonto, P. P.; Chauke, H. R.; Ngoepe, P. E. Ab Initio Studies of O₂ Adsorption on (110) Nickel-rich Pentlandite (Fe₄Ni₅S₈) Mineral Surface. *Minerals* **2015**, *5*, 665–678.
- Ntobeng, S. T.; Mkhonto, P. P.; Mehlape, M. A.; Ngoepe, P. E. In *Computational Modelling Studies of Pentlandite (Fe,Ni)₉S₈ (111) Surface: Oxidation and hydration*, Proceeding of SAIP2021, 2022; pp 43–48.
- Mkhonto, P. P.; Zhang, X.; Lu, L.; Xiong, W.; Zhu, Y.; Han, L.; Ngoepe, P. E. Adsorption Mechanisms and Effects of Thiocarbamate Collectors in the Separation of Chalcopyrite from Pyrite Minerals: DFT and Experimental Studies. *Min. Eng.* **2022**, *176*, 107318.
- Zhang, X.; Xiong, W.; Lu, L.; Qian, Z.; Zhu, Y.; Mkhonto, P. P.; Zheng, Y.; Han, L.; Ngoepe, P. E. A Novel Synthetic Polymer Depressant for the Flotation Separation of Chalcopyrite and Galena and Insights into its Interfacial Adsorption Mechanism. *Sep. Purif. Technol.* **2021**, *279*, 119658.
- Tasker, P. W. Stability of Ionic Crystal Surfaces. *J. Phys. C: Solid State Phys.* **1979**, *12*, 4977–4984.

- (33) Ratsch, C.; Barvosa-Carter, W.; Grosse, F.; Owen, J. H. G.; Zinck, J. J. Surface Reconstructions for InAs(001) Studied with Density-Functional Theory and STM. *Phys. Rev. B* **2000**, *62*, R7719.
- (34) Hohenberg, P.; Kohn, W. Density Functional Theory. *Phys. Rev. B* **1964**, *136*, 864–876.
- (35) Parr, R. G.; Weitao, Y. *Density Functional Theory of Atoms and Molecules*, Oxford University Press, 1994.
- (36) Tkatchenko, A.; Scheffler, M. Accurate Molecular Van der Waals Interactions from Ground-state Electron Density and Free-atom Reference Data. *Phys. Rev. Lett.* **2009**, *102*, 073005.
- (37) Perdew, J. P.; Burke, K.; Ernzerhof, M. Generalized Gradient Approximation Made Simple. *Phys. Rev. Lett.* **1996**, *77*, 3865–3868.
- (38) Clark, S. J.; Segall, M. D.; Pickard, C. J.; Hasnip, P. J.; Probert, M. J.; Refson, K.; Payne, M. C. First Principles Methods using CASTEP. *Z. Kristallogr. Cryst. Mater.* **2005**, *220*, 567–570.
- (39) Monkhorst, H. J.; Pack, J. D. Special Points for Brillouin-zone Integrations. *Phys. Rev. B* **1976**, *13*, 5188–5192.
- (40) Pearson, W. B. *The Crystal Chemistry and Physics of Metals and Alloys*; Wiley: New York, 1971.
- (41) Neumann, M. A. X-Cell - A Novel Indexing Algorithm for Routine Tasks and Difficult Cases. *J. Appl. Cryst.* **2003**, *36*, 356–365.
- (42) Collins, R.; Kaner, R.; Russo, P.; Wold, A.; Avignant, D. High-pressure Phase Transformation of Platinum Sulfide. *Inorg. Chem.* **1979**, *18*, 727–729.
- (43) Nguyen-Manh, D.; Ntoahae, P. S.; Pettifor, D. G.; Ngoepe, P. E. Electronic Structure of Platinum-Group Minerals: Prediction of Semiconductor Band Gaps. *Mol. Simul.* **1999**, *22*, 23–30.
- (44) Dey, S.; Jain, V. K. Platinum group Metal chalcogenides: Their Syntheses and Applications in Catalysis and Materials Science. *Platinum Met. Rev.* **2004**, *48*, 16–29.
- (45) Hulliger, F. Electrical Properties of Some Nickel-Group Chalcogenides. *J. Phys. Chem. Solids* **1965**, *26*, 639–645.
- (46) Monaghan, S.; Coleman, E. M.; Ansari, L.; Lin, J.; Buttner, A.; Coleman, P. A.; Connolly, J.; Povey, I. M.; Kelleher, B.; ÓCoileáin, C.; McEvoy, N.; Hurley, P. K.; Gity, F. Structural and Electrical Characterisation of PtS from H₂S-converted Pt. *Appl. Mater. Today* **2021**, *25*, 101163.
- (47) Leung, K.; Rempe, S. B.; Schultz, P. A.; Sproviero, E. M.; Batista, V. S.; Chandross, M. E.; Medforth, C. J. Density Functional Theory and DFT+U Study of Transition Metal Porphines Adsorbed on Au(111) Surfaces and Effects of Applied Electric Fields. *J. Am. Chem. Soc.* **2006**, *128*, 3659–3668.
- (48) Devey, A. J.; Grau-Crespo, R.; de Leeuw, N. H. Electronic and Magnetic Structure of Fe₃S₄: GGA+U Investigation. *Phys. Rev. B* **2009**, *79*, 195126.
- (49) Anisimov, V. I.; Zaanen, J.; Anderson, O. K. Band Theory and Mott Insulators: Hubbard U Instead of Stoner I. *Phys. Rev. B* **1991**, *44*, 943–954.
- (50) Liechtenstein, A. I.; Anisimov, A. I.; Zaanen, J. Density Functional Theory and Strong Interactions: Orbital Ordering in Mott Hubbard Insulators. *Phys. Rev. B* **1995**, *52*, R5467.
- (51) Berry, L. G.; Thompson, R. *M.X-ray Powder Data for Ore Minerals: The Peacock Atlas*; Geological Society of America: New York, 1962; Vol. 85, pp 1–281.
- (52) Singh-Miller, N. E.; Marzari, N. Surface Energies, Work Functions, and Surface Relaxations of Low Index Metallic Surfaces From First-Principles. *Phys. Rev. B* **2009**, *80*, 235407.
- (53) Sun, W.; Ceder, G. Efficient Creation and Convergence of Surface Slabs. *Surf. Sci.* **2013**, *617*, 53–59.
- (54) Tian, X.; Wang, T.; Fan, L.; Wang, Y.; Lu, H.; Mu, Y. A DFT Based Method for Calculating the Surface Energies of Asymmetric MoP Facets. *Appl. Surf. Sci.* **2018**, *427*, 357–362.
- (55) Santos-Carballal, D.; Roldan, A.; Grau-Crespo, R.; de Leeuw, N. H. A DFT Study of the Structures, Stabilities and Redox Behaviour of the Major Surfaces of Magnetite Fe₃O₄. *Phys. Chem. Chem. Phys.* **2014**, *16*, 21082–21097.
- (56) Cooper, T. G.; de Leeuw, N. H. A Computer Modelling Study of the Incorporation of K⁺, Ca²⁺ and Mg²⁺ Impurities in Two Na₂SO₄ Polymorphs: Introducing a Na₂SO₄ Potential Model. *J. Cryst. Growth* **2006**, *294*, 137–149.
- (57) de Leeuw, N. H.; Cooper, T. G. Surface Simulation Studies of the Hydration of White Rust Fe(OH)₂, Goethite α-FeO(OH) and Hematite α-Fe₂O₃. *Geochim. Cosmochim. Acta* **2007**, *71*, 1655–1673.
- (58) Wulff, G. Zur Frage der Geschwindigkeit des Wachstums und der Auflösung der Krystallflagen. *Z. Kristallogr. Mineral* **1901**, *34*, 449–530.
- (59) Gibbs, J. W. *The Collected Works of J. Willard Gibbs*, Longmans, Green: New York, 1928; pp 1839–1903.
- (60) Slater, J. C. Atomic Radii in Crystals. *J. Chem. Phys.* **1964**, *41*, 3199–3205.
- (61) Heiskanen, K.; Kirjavainen, V.; Laapas, H. Possibilities of Collectorless Flotation in the Treatment of Pentlandite. *Ores. Int. J. Miner. Process.* **1991**, *33*, 263–274.
- (62) Kelebek, S.; Nanthakumar, B. Characterization of Stockpile Oxidation of Pentlandite and Pyrrhotite Through Kinetic Analysis of their Flotation. *Int. J. Miner. Process.* **2007**, *84*, 69–80.